THE AMAZON HYDROMETEOROLOGY: CLIMATOLOGY, VARIABILITY AND LINKS TO CHANGES IN WEATHER PATTERNS

A Dissertation
Presented to
The Academic Faculty

by

Kátia de Ávila Fernandes

In Partial Fulfillment
of the Requirements for the Degree
Doctor of Philosophy in the
School of Earth and Atmospheric Sciences

Georgia Institute of Technology
December, 2009

THE AMAZON HYDROMETEOROLOGY: CLIMATOLOGY, VARIABILITY AND LINKS TO CHANGES IN WEATHER PATTERNS

Approved by:

Dr. Rong Fu, Advisor
School of Earth and Atmospheric Sciences
Georgia Institute of Technology

Dr. Marc Stieglitz
School of Earth and Atmospheric Sciences
Georgia Institute of Technology

Dr. Peter J. Webster
School of Earth and Atmospheric Sciences
Georgia Institute of Technology

Dr. Robert E Dickinson
Jackson School of Geosciences
The University of Texas at Austin

Dr. Robert X. Black
School of Earth and Atmospheric Sciences
Georgia Institute of Technology

Date Approved: July 13th, 2009

ACKNOWLEDGEMENTS

I wish to acknowledge the invaluable guidance, friendship and encouragement I received from my advisor Dr. Rong Fu, without which this work could not be done. I am grateful for the advisement, help and support always kindly offered to me by Dr. Robert Dickinson.

I also thank Dr. Alan K. Betts for immeasurable contributions to my studies and professional growth and Dr. Peter Webster for always making himself available for consultation. I am grateful to Dr. Robert Black and Dr. Marc Stieglitz for serving as my thesis committee and for invaluable suggestions and comments. I thank Dr. Greg Huey for his encouragement and teachings during my time working as his Teaching Assistant.

Acknowledgements are due to my colleagues Wenhong Li, Robinson Negrón Juárez, Huilin Gao, Yan Zhang, Jon Wright, Marilee Roell and Paola Arias who provided inspiration, encouragement and professional collaboration during my time at Georgia Tech. I wish to thank Susan Ryan, Kathy Plummer, Rita Anderson and Laura Cederquist for their support and efficient assistance during my time at Georgia Tech. My work could not have been done without the invaluable help and courtesy I received from Mark Keever, Angelica Remolina and Chris Lowell.

Very special thanks go my parents for their support and for instilling in me from early age the value of education. I also thank my friends, who despite my repeated refusal to socialize with them throughout my graduate years, are still supportive and present.

Finally my husband-Sergio Bernardes' love, dedication and encouragement made my journey much smoother. Beyond emotional support I am thankful to him for technical contributions and discussions.

TABLE OF CONTENTS

LIST OF TABLES

LIST OF FIGURES

LIST OF SYMBOLS AND ABBREVIATIONS

CAI	Cold Air Incursion
CPC	Climate Prediction Center
DJF	December-February
DMI	Dipole Mode Index
EC	Expansion Coefficient
ENSO	El Niño Southern Oscillation
ERA40	European Centre for Medium Range Weather Forecast 40 years Reanalysis
ET	Evapotranspiration
GCM	Global Climate Model
GPCP	Global Precipitation Climatology Project
JJA	June -August
LBA	Large-Scale Biosphere Atmosphere
O+A	Óbidos plus Altamira
ONI	Oceanic Niño Index
P	Precipitation
PDO	Pacific Decadal Oscillation
PSA	Pacific South American
R	Runoff
SLP	Sea Level Pressure
SON	September –November
SST	Sea Surface Temperature
SVD	Singular Value Decomposition

TRMM	Tropical Rainfall Measuring Mission
θe	Equivalent Potential Temperature
θes	Saturation Equivalent Potential Temperature
σ	Standard Deviation

SUMMARY

My thesis focuses on improving the quantification of the hydrological cycle and understanding the atmospheric processes that link weather to climate in the Amazon River basin. By using ERA40 and independent observations, I assess how well we can estimate the surface water budget in the Amazon River basin. I find that ERA40 basin wide annual precipitation (P) overall agrees with observations showing a slight underestimation of 10% in average, whereas runoff (R) is underestimated by a larger margin (~25%). Observed residual of precipitation and runoff (denoted as P-R) is better estimated by ERA40 P-R than actual ET which includes soil moisture nudging.

The causes for said discrepancies were found to partly relate to soil moisture nudging that needs to be applied during the dry season to produce realistic ET and compensate for the low soil moisture recharge during the previous wet season. Insufficient recharge may in part be caused by underestimation of rainfall amount and intensity; moreover the shallow root layer in the model does not represent the deep soil water reservoir characteristic of the Amazonian forest.

Whether the hydrological cycle and weather patterns in the Amazon have changed during the past few decades is a highly debatable but central question for detecting climate change in the region. The second part of my thesis focus on the physical links between rainfall changes detected in observations, and changes of synoptic scale systems as represented by ERA40. My results suggest that an observed delayed wet season onset is consistent with a decreasing number of cold air incursion (CAI) days in southern Amazon for the period 1979-2001.

The variability of CAI into southern Amazon is related to the variability of SST upstream of South America in the tropical Pacific and Indian Oceans. A Singular Value Decomposition Analysis (SVD) between CAI days and global SST reveal three main modes of co-variability. The first mode describes the effect of the El Niño-Southern Oscillation. During El Niño (La Niña) a strong (weak) subtropical jet stream over South America tends to prevent transient systems from moving to southern Amazon, resulting in decreased (increased) CAI days during SON. The second mode of co-variability shows an anomalously warm western Indian Ocean also related to strong subtropical jet stream, except the jet is positioned farther north in South America, which along with the absence of a well defined subpolar jet stream, favors the northward displacement of transient waves into central South America, but show little response in southern Amazon. The CAI days reconstructed from the first and second modes do not present any significant trend in southern Amazon. CAI days reconstructed from the third mode of co-variability on the other hand, reproduces the SON observed trend in almost its entirety. The third mode of co-variability describes negative (positive) anomalies in CAI days associated with cold (warm) SST anomalies in the eastern tropical Pacific, anomalous wavetrain in the Southern Hemisphere and Walker Cell displacement that are unfavorable (favorable) to the incursion of CAI into southern Amazon. The temporal evolution of this mode correlates negatively with the Pacific Decadal Oscillation, suggesting that the recent gradual shift in PDO polarity reflected on the interannual response of Southern Pacific atmospheric patterns, hence on the behavior of transients propagation. The negative PDO index and its related atmospheric patterns are in agreement with the reduced observed CAI days, which also related to a delayed wet season onset in the southern Amazon.

CHAPTER 1

INTRODUCTION

1.1 Background

The Amazon is an important component of the global climate system, mainly due to its role in the water, energy and carbon cycling. Convection over Amazonia is the second greatest source of diabatic heat that drives atmospheric circulation in the tropics, especially in the western hemisphere. Its main river- the Amazon- pours eighteen percent of the global fresh water discharge into the oceans, an amount greater than the sum of the next eight world's greatest rivers discharge [*Dai and Trenberth*, 2002]. Rainfall also nourishes about 10 to 15% of global terrestrial biomass and a quarter of the global biospecies [*Field et al.*, 1998]. Consequently precipitation variability is closely related to the variability of global atmospheric CO_2 [*Ometto et al.*, 2005; *Tian et al.*, 1998].

The interannual precipitation variability in the Amazon is often related to its seasonal onset timing, which is controlled by local land surface processes and large scale mechanisms [*Fu et al.*, 1999; *Fu and Li*, 2004; *Li and Fu*, 2004; 2006; *Liebmann and Marengo*, 2001; *Marengo et al.*, 2001]. On regional scales, an increase in the frequency of cross-equatorial northerly winds tends to lead the wet season onset, indicating the importance of moisture transport from the Atlantic to the onset region [*Fu et al.*, 2001; *Wang and Fu*, 2002]. Locally, anthropogenic biomass burning during the transition from dry to wet season in southern Amazon works to stabilize the lower troposphere. The smoke aerosols reduce the surface solar flux and stabilize the lapse rate, slowing down or weakening the normal monsoon transition [*Bevan et al.*, 2009; *Yu et al.*, 2007; *Zhang et al.*, 2008; *Zhang et al.*, 2009]. Extratropical synoptic systems are also important

triggering mechanisms of the wet season onset, as demonstrated by *Li and Fu* [2006]. The authors also suggest that late wet season onset may be related to episodes of El Niño, when the subtropical jet stream over the southern Pacific and South America is stronger preventing cold fronts from reaching southern Amazon.

In the context of global climate change, some modeling studies have projected an increase in atmospheric CO_2 in the 21st century as a result of a projected Amazon rainforest die back [*Cox et al.*, 2004; *Fung et al.*, 2005], although whether this die back would occur is highly uncertain due to large discrepancies in projected future rainfall change in the Amazon [*Li et al.*, 2006]. Observational studies have shown a clear trend towards higher temperatures in the Amazon especially over the last 3 decades [*Hansen et al.*, 2006; *Malhi and Wright*, 2004]. On the other hand, trends in annual precipitation are not as clear [*Costa and Foley*, 1998; *Haylock et al.*, 2006; *Marengo*, 2004; *Wang and Ding*, 2006], even though changes in drought frequency and seasonal cycle of precipitation have been observed in recent studies [*Bevan et al.*, 2009; *Cox et al.*, 2008; *Li et al.*, 2008].

1.2 Motivation, Objectives and Outline

Estimating the surface water budget in the Amazon is a challenge due mainly to the lack of adequate observational network. The advances of remote data acquisition and assimilation into reanalyses products have greatly reduced that deficiency in the past few decades. By comprehensively using independent observations and the European Centre for Medium-Range Weather Forecast (ECMWF) reanalysis (ERA40) product, my thesis work addresses how well we can currently estimate the Amazon surface water budget. Global Climate Models (GCMs) reanalysis are often used as pseudo-observations for

validation, verification and initialization of regional models [*Betts et al.*, 2003; *Betts et al.*, 2005; *Coe*, 2000; *Hagemann and Gates*, 2003; *Roads and Betts*, 2000]. Therefore, a clear understanding of the strengths and weaknesses of ERA40 water budget variables becomes necessary information to scientists studying the Amazon hydrometeorology. The study presented in Chapter 2, aims to assess and improve observational characterization of the water cycle and related atmospheric processes in the Amazon River basin using both observations and atmospheric reanalysis product. In doing so, I aim to provide a more reliable observational basis for understanding past climate variability and the underlying processes, which, in turn, can be used to evaluate and constrain global climate models (GCM) and their predictions for future climate change. This part of my thesis has been published in the Journal of Geophysical Research [*Fernandes et al.*, 2008].

Whether the hydrological cycle in the Amazon has changed during the past few decades is a highly debatable question for detecting climate change in the region. Both rainfall data and reanalysis products alone may not be reliable in resolving decadal scale changes especially in regions sparsely monitored like the Amazon. However, the consistency between rainfall and atmospheric dynamic fields on synoptic scale changes in southern Amazon shown in previous studies [*Garreaud*, 1999; *Oliveira*, 1986] suggest that these data and products are adequate for studying weather patterns. Thus, my analysis presented in Chapter 3, focuses on the physical consistency between interannual and decadal changes of synoptic weather patterns as represented in ERA40 and changes in the wet season onset in southern Amazon. Previous studies have suggested that the leading edge of cold air masses in southern Amazon introduce lower troposphere

convergence and are related to the wet season onset in more than 70% of the seasons [*Li and Fu*, 2006]. However, whether cold air incursions have changed spatially and temporally and if so, how it could contribute to changes the southern Amazon wet season onset have not been explored in literature.

In Chapter 4, the links between changes in cold air incursion frequency and spatial pattern and dominant modes of tropical interannual variability are explored and discussed in terms of mechanisms.

In Chapter 5, I summarize the results of my thesis and discuss their contribution to the characterization and understanding of the Amazon hydrometeorology variability and change. Proposed future work is also presented.

CHAPTER 2

THE AMAZON HYDROLOGICAL CYCLE IN THE EUROPEAN CENTRE FOR MEDIUM RANGE WEATHER FORECAST REANALYSIS (ERA40)

2.1 Introduction

The reanalysis products produced by global forecast and analysis systems that assimilate observations have increasingly been used for validation, verification and initialization of regional models, as well as for diagnostic studies of atmospheric and hydrological processes [*Betts et al.*, 2003; *Betts et al.*, 2005; *Coe*, 2000; *Dai and Trenberth*, 2002; *Hagemann and Gates*, 2003; *Lenters et al.*, 2000; *Roads and Betts*, 2000; *Seneviratne et al.*, 2004; *Zeng*, 1999]. The European Centre for Medium-Range Weather Forecasts (ECMWF) reanalysis, known as ERA40, is regarded as one of the best available reanalysis products. It is particularly useful for studies in areas that lack an adequately dense observational data network, such as the Amazon River basin.

However, *Betts et al.* [2005] find that errors in the atmospheric moisture analysis resulted in spurious decadal changes of ERA40 precipitation and runoff. The authors propose a correction that removes these large errors, but the inter-annual variability is poorly correlated with observations in the Amazon. *Marengo* [2005], using the National Centers for Environmental Prediction (NCEP) reanalysis, suggest that the non-closure of the water cycle budget may mean that this reanalysis does not realistically represent these fields over the Amazon Basin.

How well ERA40 hydrometeorological variables agree with observations on seasonal, annual, and interannual scales as well as a diagnostic analysis of possible causes for the discrepancies between the reanalysis and observations are examined in this Chapter. The role of soil moisture nudging in maintaining evapotranspiration through the dry season is also assessed.

2.2 Data and Methods

2.2.1 ECMWF Reanalysis (ERA40)

ERA40 reanalysis data are available at a spatial resolution of 2.5^{o} latitude by 2.5^{o} longitude on the ECMWF website. The reanalysis project also generated basin-averaged data subsets designed to study the hydrometeorology of 31 river basins in the world. The Amazon River basin in ERA40 is divided into 5 sub-basins with a total area of 5.71 million km^2 (Figure 2.1). These sub-basins are Rio Tapajós-Xingu, Madeira, Solimões, Negro, and the fifth basin includes several tributaries to the Amazon including the Juruá and Purus Rivers. These data are composed of twice-daily segments of the 0-12, 12-24, 24-36 hour forecasts (FX). For this study the 0-12 FX data were used, because the time needed for precipitation spin-up/spin-down is small for the Amazon [*Betts et al.*, 2005]. For the entire Amazon Basin, the seasonal cycle of ET, P-R and the ERA40 soil moisture analysis increment were calculated by weighting each basin with its partial area.

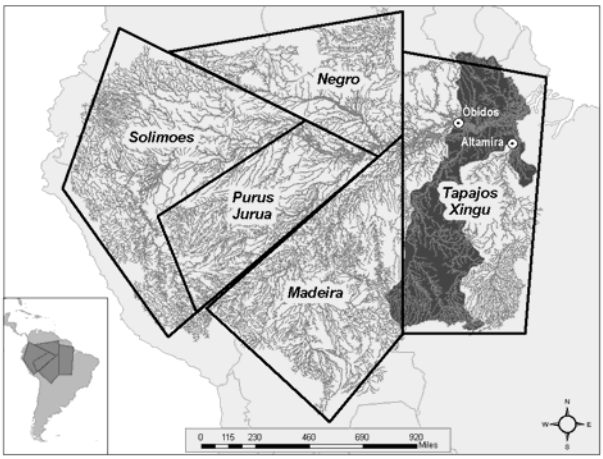

Figure 2.1. The drainage areas of the Amazon River and its main tributaries, and the locations of the Óbidos and Altamira river flow gauges. The dark gray shade represents the ungauged portion of the basin.

For the basin-wide comparison of ERA40 with observations, the gridded data were averaged over the catchment areas of the Óbidos and Altamira streamflow gauges. This excludes the Tapajós River basin, which is ungauged (see section 2.2.2). The hydrological years, from September to August of the following year, are used to compute annual means, and to examine the seasonal cycle between the period of 1980 and 2002, when both river discharge and precipitation data are available. For the evaluation of ERA40 ET against flux tower data, a special ERA40 output for single 1.25˚x1.25˚ grid-points that overlap each flux tower were used.

2.2.2 Observational data

The ERA40 data do not have river routing information, so the runoff can be compared to observed streamflow only when it is integrated over the annual cycle for the entire upstream drainage area relative to the streamflow gauges. This is because the mean residence time of runoff can be up to five months in the Amazon River basin [*Chapelon*

et al., 2002; *Marengo*, 2005]. Two streamflow gauge stations, Óbidos (1.9°S, 55.46°W) and Altamira (3.2°S, 52.2°W), hereafter referred to as O+A, cover about 5.12 million km^2 or 90% of the Amazon River basin. The Óbidos station monitors flow from most of the Amazon River basin including major tributaries such as the Solimões, Madeira, Purus-Juruá, and Negro Rivers. Altamira measures the flow from the Xingu River. The only major tributary not represented in these data is the Tapajós River to the south of the Amazon River main stem, roughly corresponding to the western half of the box labeled as Tapajós-Xingu in Figure 2.1.

ERA40 precipitation was compared with two observational datasets. These are the Global Precipitation Climatology Project (GPCP-Version 2) [*Adler et al.*, 2003] and the Global Land Precipitation by the Climate Prediction Center (CPC) [*Chen et al.*, 2002], hereafter referred to as GPCP and CPC respectively. GPCP uses precipitation estimated from the Special Sensor Microwave/Imager data on polar-orbiting multi-satellites to calibrate precipitation estimated from the infrared brightness temperatures measured by geostationary satellites. The satellite estimated precipitation is also calibrated by the rain-gauge analysis [*Adler et al.,* 2003]. The gauge-only CPC method consists of defining the analysis value at a grid point by modifying a first-guess field with the weighted mean of the differences between the observed values and the first-guess values at station locations within a searching distance. A 10-year precipitation mean is used as the first guess, and the searching distance is set to 300 km [*Chen et al.*, 2002]. Observed basin-mean rainfall is calculated for the O+A catchments using these two rainfall datasets.

Direct measurement of ET is only available at a few sites in the Amazon, and these have relatively short time-series. We use data from three Large-Scale Biosphere

Atmosphere (LBA) Experiment flux towers and from one that precedes LBA. These are respectively the Floresta Nacional do Tapajós - km83, Manaus - km34, Reserva Biológica de Jaru, and Reserva Ducke-Manaus towers. We also used the ET values at the Reserva Biológica de Cuieiras, taken from *Malhi et al*.[2002]. Table 2.1 lists the location, period of experiment and vegetation type for each flux tower. The flux towers at Manaus, Cuieras, and Ducke are located within the same grid-point in ERA40. All flux towers are located in undisturbed primary forest, except for the Tapajós tower site, where selective logging occurred about one year after the tower installation.

Table 2.1. The locations, experiment periods and types of surrounding vegetation for the flux towers used in this analysis. Names by which the towers are referred to in the text are in parenthesis.

Flux Towers	**Location**	**Years**	**Site Description**
Floresta Nacional do Tapajós-km 83 **(Tapajós)**	3°S, 55°W	2001 and 2002	Primary Forest, selectively logged in Sep 2001.
Manaus-km 34 **(Manaus)**	2.5°S, 60°W	2000 and 2002	Primary Forest
Reserva Biológica de Jaru **(Jaru)**	10.1°S, 61.9°W	2001 and 2002	Primary Forest
Reserva Ducke Manaus **(Ducke)**	2.5°S, 60°W	1984 and 1985	Primary Forest
Reserva Biológica de Cuieiras **(Cuieiras)**	2.5°S, 60°W	1996	Primary Forest

Runoff in ERA40 is primarily deep runoff or base flow, which increases rapidly once soil water in the 1 to 2.9 m soil layer exceeds some threshold greater than the field capacity. Surface runoff almost never occurs in ERA40 unless the soil is frozen. Infiltration of rainfall to the deep soil depends on the soil hydraulic properties, which are assumed uniform globally. Precipitation throughfall, which is determined by precipitation

minus canopy interception loss, is computed in ERA40 based on the model proposed by *Rutter et al.* [1975]. The amount of water intercepted by vegetation varies with the leaf area index and the intensity of rainfall. A greater percentage of rainfall is intercepted by the forest canopy during an episode of light rain than during a storm with heavy rain. Interception loss in ERA40 is however not readily available to users, nor is it available from observations on the basin scale. So instead the intensity of rain is evaluated in this study as a proxy for throughfall.

To estimate rain-rate, the TRMM 3B42V6 product merged passive microwave precipitation estimates/infrared precipitation product is used [*Adler et al.*, 2000; *Kummerow et al.*, 2000]. These data were derived from the combined instrument rain calibration algorithm (3B42), which uses intercalibrated passive microwave estimates, microwave-adjusted infrared estimates from geostationary satellites, and adjustments to monthly gauge data. The TRMM rain-rate 3B42V6 product is available at a spatial resolution of 0.25^{o} every three hours in units of millimeters per hour. Rain-rates from these data were binned to 2.5^{o} and six-hour resolutions to match those of ERA40. We then compare ERA40 and TRMM by calculating the cumulative probability density functions for the hourly rain-rates at each grid for the entire domain of 80^{o}W-40^{o}W and 20^{o}S-5^{o}N and the period January 1st 1998 to August 31st 2002 when ERA40 and TRMM data overlap.

2.3 Results

2.3.1 Precipitation

Figure 2.2 shows the basin-mean annual precipitation in ERA40 compared with the GPCP and CPC datasets. Annual rainfall in ERA40 is on average 3% greater than

that estimated by GPCP, but 10% less than that estimated by the CPC dataset. Thus, ERA40 falls within the uncertainty of the observations. Rainfall in the GPCP dataset after 1986 is calibrated by rain-gauges from the Global Precipitation Climatology Centre (GPCC) data [*Adler et al.*, 2003]. The ten-year mean annual rainfall of the GPCC dataset is as much as 2 mm day^{-1} lower than that of the CPC over tropical South America [*Chen et al.*, 2002], leading to a lower annual rainfall in the GPCP data. However, which rainfall dataset more realistically represents the actual annual rainfall remains unclear. Additional constraints from other independently measured variables in the surface water budget will be discussed later in this Chapter to explore this question.

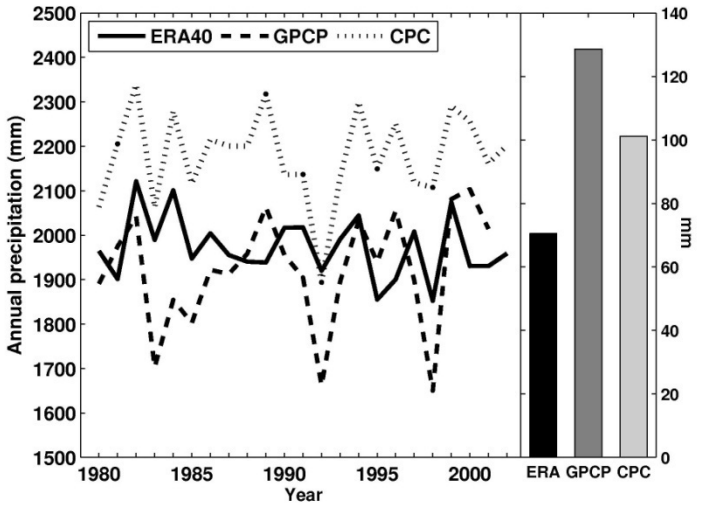

Figure 2.2. Basin-averaged annual rainfall in ERA40, CPC, and GPCP datasets. The bars on the right represent annual standard deviation for ERA40, GPCP and CPC respectively.

Interannual variations of basin-averaged rainfall in the Amazon, shown as standard deviation bars on the right-hand-side in Figure 2.2, are generally within 7% of the annual mean for the period of this study, with the greatest deviations during El Niño-

Southern Oscillation (ENSO) episodes. The years of 1983, 1992, and 1998 were strong El Niño years and were associated with the lowest observed precipitation, except for the CPC precipitation in 1998. The years 1989 and 1999 are among the highest annual precipitation totals in the series, consistent with strong La Niña episodes [*Neelin et al.*, 1998; *Ropelewski and Halpert*, 1987]. The interannual variations of the two observational data sets are more highly correlated than either of them is to the interannual time-series of ERA40. The reanalysis tends to underestimate the interannual variability by overestimating precipitation for El Niño (e.g.1992) and underestimating La Niña (e.g. 1989 and 1999) episodes, when compared to observations. 1992 was the only year when ERA40 produced more rain than both the GPCP and the CPC datasets.

How well ERA40 captures the seasonal cycle of rainfall is evaluated in Figure 2.3. The phase of the ERA40 seasonal cycle agrees well with observations. The amplitude of the rainfall seasonal cycle is however underestimated compared to both GPCP and CPC, showing, respectively, a low bias of 4% and 11% or 9 to 25 mm per month during the wet season (December to March). From the middle of the dry season (July) to the end of the transition season (November), the rainfall amounts in ERA40 agree with the CPC data, but they are as much as 22% (or 20 mm/month) higher than the GPCP data.

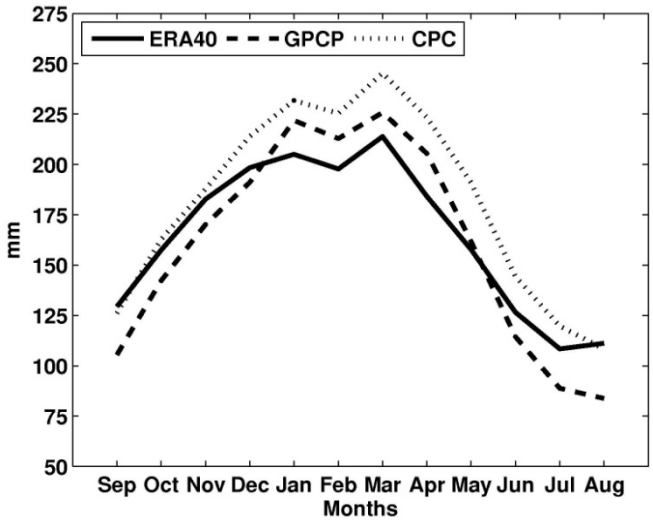

Figure 2.3. The mean annual cycle of ERA40, GPCP, and CPC precipitation for the period 1980-2002.

The spatial distribution of rainfall is investigated in Figure 2.4 for December to February (DJF) and June to August (JJA), by subtracting the CPC precipitation from that of ERA40. During DJF, rainfall in ERA40 is on average lower than CPC (shaded areas in Figure 2.4) over most of the Purus-Juruá, Madeira, and Tapajós-Xingu sub-basins. The low biases of rainfall in these basins are the main contributor to the underestimation of basin mean rainfall during the wet season (Figure 2.3). During the dry season, however, ERA40 rainfall is higher (lower) than that of the CPC by as much as 300 mm in parts of the Purus-Juruá and Madeira River (Negro and Solimões River). Figure 2.4 suggests that the sub-basin rainfall may have larger percent errors than the Amazon basin average.

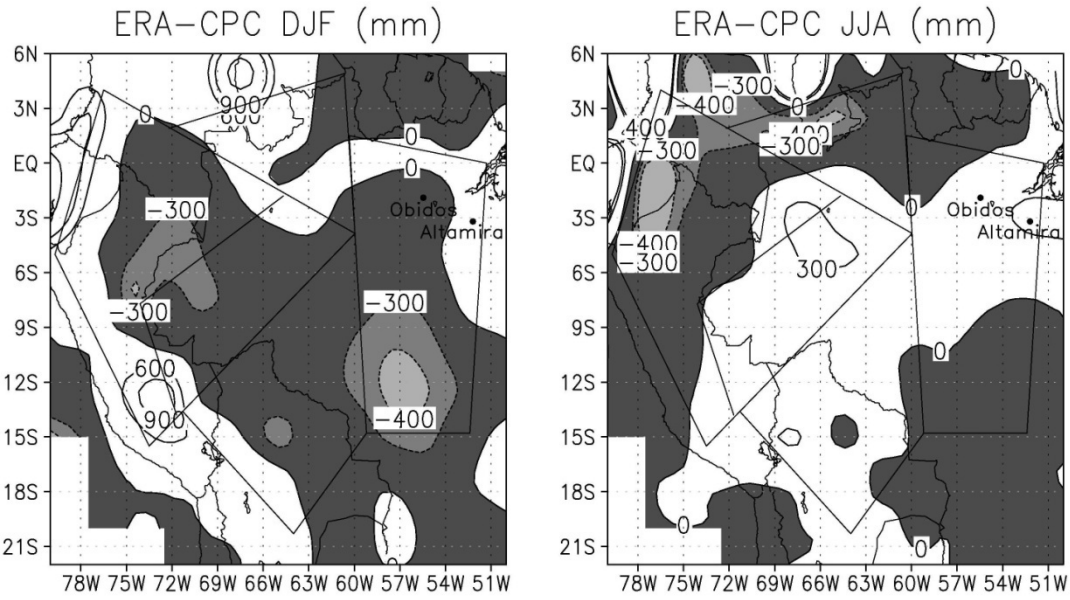

Figure 2.4. The differences between ERA40 and CPC for the mean seasonal total precipitation for the period 1980-2002 (Unit: mm). The left panel shows the wet season (DJF) and the right panel shows the dry season (JJA). The polygons represent the five Amazon sub-basins in ERA40. The areas where ERA40 rainfall is lower than that of CPC (negative difference) are shaded.

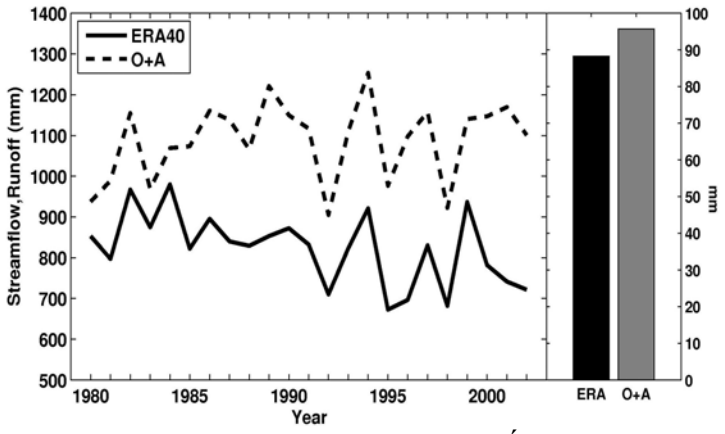

Figure 2.5. The annual stream flow measured at Óbidos and Altamira, and the corresponding mean runoff for the same drainage area in ERA40 (Unit: mm). The bars on the right-hand side indicate the standard deviations of annual runoff in ERA40 and the observed streamflow.

2.3.2 Runoff and Rainrate

Figure 2.5 shows basin-averaged runoff compared to total river discharge at the streamflow gauges of Óbidos and Altamira, both near the mouth of the Amazon (Figure 2.1). The bars on the right-side of Figure 2.5 represent the standard deviations of ERA40 and observed annual runoff. ERA40 annual runoff underestimates river streamflow by 25% on average for the period of 1980-2002. ERA40 also shows a small decrease in runoff during the 1990s compared to the 1980s, while the streamflow observations show no clear trend. Some of this spurious interannual variability in runoff and precipitation in ERA40 is maybe related to problems with the atmospheric moisture analysis [*Betts et al.*, 2005]. Clearly, however, the runoff fraction is underestimated in the reanalysis.

To explore whether errors in the ERA40 runoff might be influenced by inadequate throughfall, we compare rainfall intensity between ERA40 and TRMM observations. In densely vegetated areas, a significant amount of precipitation may stay on the leaves and evaporate. A single storm can saturate the canopy very quickly, whereas drizzle tends to produce a greater interception loss fraction for the same total rainfall. Therefore, an adequate estimate of precipitation intensity, as well as a realistic model for the interception loss, is important to simulate throughfall.

Figure 2.6 compares the cumulative probability density function for the 2.5˚ grid 6-hourly rainrate between ERA40 and TRMM. The values of rainrate are lower than those reported in literature [*Anagnostou and Morales*, 2002; *Cutrim et al.*, 2000] due to the lower spatial and longer temporal resolutions used in this analysis that are constrained by the ERA40 rainfall output. The results indicate a lower frequency of occurrence of lighter rain and higher occurrence of relatively heavier rain in ERA40 compared to the

TRMM data, consistent with the results of *Huffman et al.* [2007] that shows underestimation of light rain in TRMM. However, the 2.5^{o} resolution of these ERA40 data is too coarse to resolve the actual rain-rate at the spatial scale of convective systems (~ 10 km to 100 km). An earlier study [*Betts et al.*, 2006], which compared ERA-40 evaporation with flux tower data over the boreal forest, suggested that ERA40 might have too much evaporation off wet canopies, but we cannot assess this with these rain-rate data.

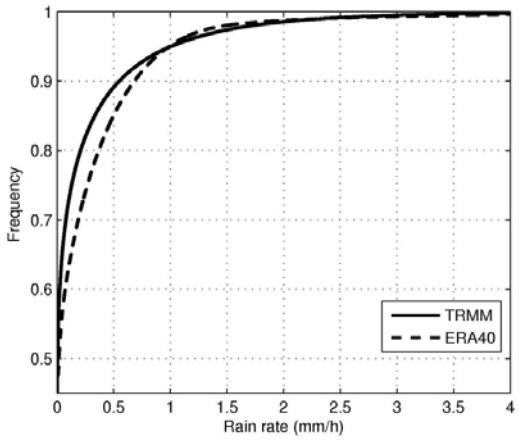

Figure 2.6. The cumulative distribution function of hourly rainrate for the 2.5˚grids for ERA40 and TRMM data. Unit: mm/h.

2.3.3 Evapotranspiration

Evapotranspiration (ET) is one of the most poorly observed variables in the atmospheric water budget. Reanalyses have been used as a surrogate for observed ET in previous studies of the hydrological cycle and wet season onset in the Amazon [*Eltahir and Bras*, 1994; *Li and Fu*, 2004; *Rao et al.*, 1996]. In this study, ERA40 ET is evaluated

against the ET measured at the flux tower locations in the eastern, central, and southern Amazon.

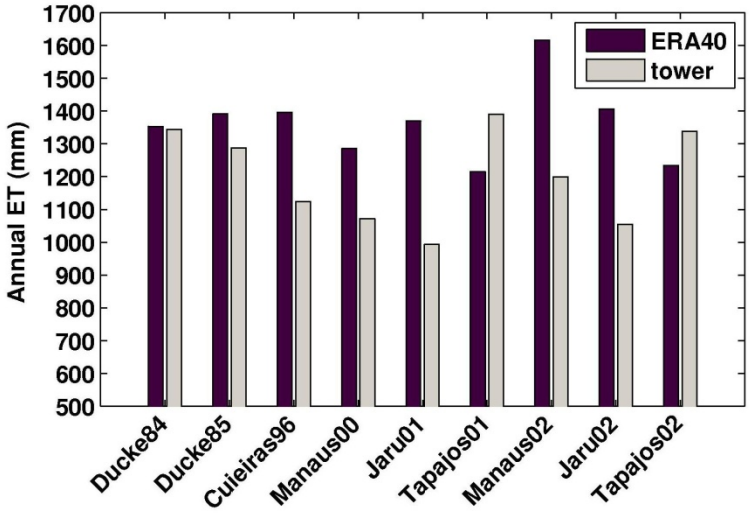

Figure 2.7. Comparison between the annual ET at ERA40 grid-points, co-located with flux tower measurements, showing the locations (see Table 2.1) and the year(s) of the field experiments. Unit: mm.

Figure 2.7 shows the annual mean ET for the periods and locations listed in Table 2.1. ET at these sites is measured by the eddy-covariance method, which is the most direct and accurate method available. The ET values are consistent with those previously estimated for the Amazon [*Eltahir and Bras*, 1994; *Matsuyama*, 1992; *Vorosmarty et al.*, 1996]. Although ET in ERA40 agrees with ET measured in the 1980s, it appears to have 15%-30% high bias compared to later observations in central and southern Amazon. Does this result suggest a possible overestimation of ET by ERA40? It is important to note that the sum of the surface latent and sensible fluxes measured by the eddy-covariance method can be 10% to 30% lower than surface net radiative flux [*Finnigan et al.*, 2003; *von Randow et al.*, 2004]. For example, *Foken et al*. [2006] estimated that the

lack of energy closure implies a possible ET underestimation of about 15%. However, *Malhi et al*. [2002] showed that energy balance closure for the Cuieiras site was within 5% for time scales longer than 4 hours, suggesting a high confidence in flux measurements for that site. ET in ERA40 agrees with observations within the observational uncertainty of 15% at Ducke and Tapajós in the equatorial central and eastern Amazon. However, at Jaru, Cuieiras, and Manaus in the southern and central Amazon, the ERA40 reanalysis overestimates ET beyond the data uncertainty. The seasonal cycle of the ET shown in Figure 2.8 suggests a systematically higher ERA40 ET in all seasons compared to the observations. However, the limited sample size and large variability of the ET measurements prevent us from determining whether the differences are significant or not.

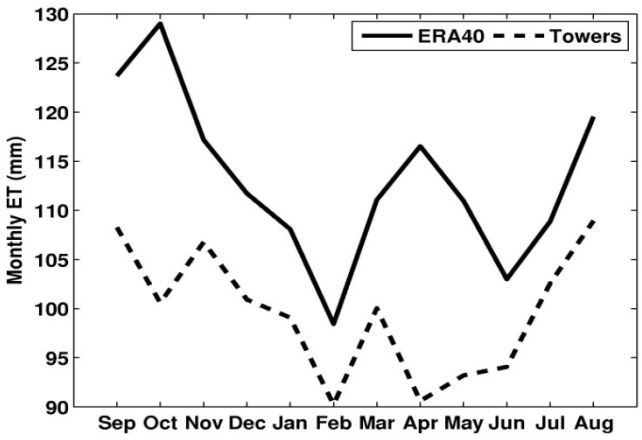

Figure 2.8. Mean seasonal cycle of ET for ERA40 and flux tower measurements, derived from data shown in Figure 2.7

In ERA40, increments of soil moisture (and first-layer soil temperature) are added based on the differences between simulated and observed screen-level humidity and temperature [*Douville et al.*, 2000]. These increments effectively nudge the soil moisture

to maintain a model ET that gives a more realistic screen-level diurnal cycle of humidity and temperature. In the dry season, the addition of soil water is substantial.

The difference between annual basin-mean P and R (denoted as P-R) would closely balance ET in the absence of soil moisture nudging. Figure 2.9 compares (P-R) with the actual ET in ERA40, and with the observed (P-R) derived from the CPC precipitation data and the streamflow gauge data. The difference between the actual ET and P-R in ERA40 indicates how much water has been added as soil moisture increments on the annual time scale. The annual P-R in ERA40 agrees overall with that observed, although ERA40 underestimates both rainfall and runoff compared to the CPC data and streamflow measurements. The actual ERA40 ET is about 10% higher than the ERA40 P-R over the study period, similar to the average 10% high bias when compared to the flux tower measurements (Figure 2.7). The overestimation of annual ET relative to both the ERA40 and observed P-R, and to the flux tower ET, suggests that the soil moisture nudging may be one of the causes. In particular, while nudging leads to a good agreement with the ET measurements at the Ducke and Tapajós towers, it overestimates ET in other sites especially in the southern Amazon (Figure 2.7).

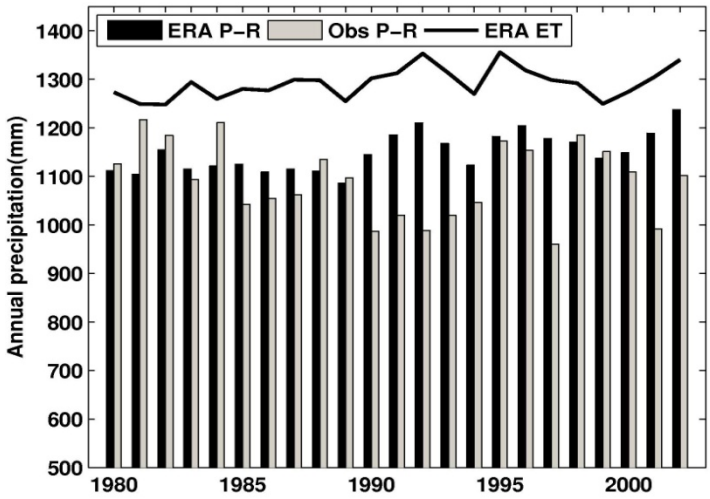

Figure 2.9. ERA40 ET compared with the time-series of the annual mean P-R in ERA40 and that derived from the CPC and river flow gauges for the period of 1980 to 2002.

Figure 2.10 shows the mean annual cycle of ERA40 P-R and ET for the period 1980-2002 along with the mean annual cycle of the soil moisture increments for the same period (but excluding the years 1989 to 1994 for which the 06 and 18UTC forecast are missing from this basin archive). The surplus of P-R over ET, which is available to recharge the soil moisture storage during the wet season (November to February), is about 45 mm. This is only about 28% of the 162 mm needed to maintain a realistic ET during the dry season, as indicated by the deficit of P-R relative to ET during the period from April to September. Hence extra water has to be added to the soil in the dry season. The annual budget of P-R relative to ET shows a deficit of about 123 mm, which is mostly compensated by the soil moisture nudging (113 mm per year).

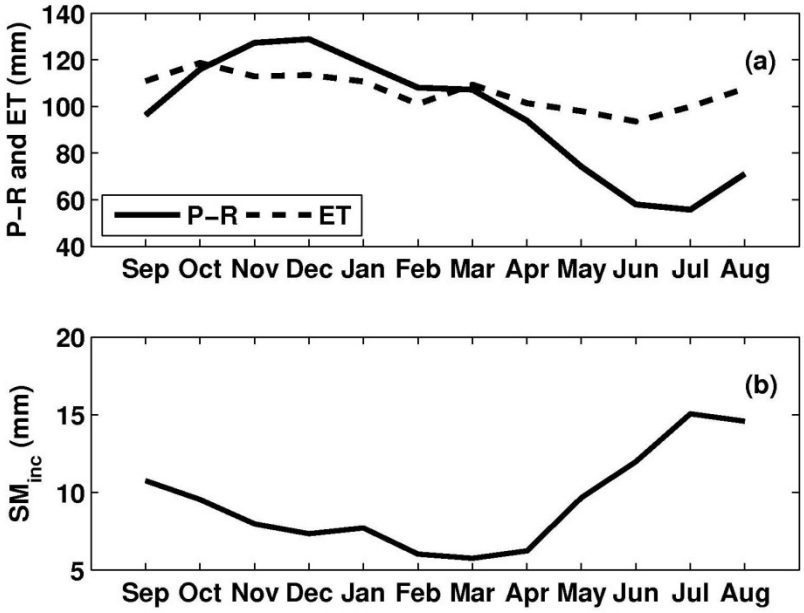

Figure 2.10. The mean seasonal cycle of (a) P-R and ET and (b) the soil moisture increment SM_{inc} in ERA40.

Observations, on the other hand, suggest that the soil moisture recharge during the wet season is sufficient to maintain dry season ET, even when the dry season rainfall is reduced to more than 50% of its normal value [*Juarez et al.*, 2007]. Thus insufficient recharge of the soil moisture storage during the wet season is probably the main cause of the insufficient soil moisture supply during the dry season, and the subsequently large soil moisture nudging in the reanalysis. It is also possible that the model interception may have a high bias [*Betts et al.*, 2006], which contributes to the high ET in the rainy season, and reduces the wet season storage. Another issue is that the soil water reservoir in ERA40 is only 2.89 m deep, and most of the roots are located in the first meter. In contrast, *von Randow et al.* [2004] that the forest drawdown of soil water in the dry season is almost as large for the 2-3.4m layer as for the 0-2m layer. Thus a shallow rooting layer may contribute to a lower seasonal soil moisture storage capacity in ERA40.

2.3.4 The annual mean water budget

Due to the lack of basin-scale ET observations and the discrepancies between different rainfall datasets, the research community was previously unable to balance the water budget for the Amazon River basin [*Marengo*, 2005]. To address this problem, we explore an alternative way to infer basin-scale ET, and determine how well we can balance the water budget for the Amazon River basin using available information. Currently, ET measured by the eddy covariance method at flux towers is considered the most reliable estimate of ET, but these ET measurements are only available at a few sites in the Amazon River basin. ERA40 represents the large-scale patterns of the atmosphere for the whole basin, but may have a bias in its ET values. Using the datasets in Figure 2.7, the annual ET at the flux tower sites ($ET_{obs,towers}$) and at the corresponding ERA40 grid boxes ($ET_{ERA40,towers}$) are averaged and used a ratio between them to calibrate the basin mean ET of ERA40 ($ET_{ERA40,\ basin}$) to give a simple climatological estimate of annual basin ET, corrected to these flux tower observations ($ET_{obs,basin}$). That is,

$$ET_{obs,basin} = ET_{obs,towers} \frac{ET_{ERA40,basin}}{ET_{ERA40,towers}} \quad (1)$$

Clearly, the time-series of in-situ ET observations are too short to estimate climatological annual ET. However, *Juarez et al.* [2007] have shown that the seasonal and interannual changes of ET at a given location are less than 12%. Their analysis was based on in-situ measurements of ET obtained during the past two decades across different parts of the Amazon rainforest areas with very different rainfall climatologies. Thus the annual ET estimate based on in-situ data in Equation (1) is probably a reasonable approximation of the climatological annual ET for the last two decades

covered by our ERA40 reanalysis, although it is likely to have the same low bias of order 10% as the flux tower measurements.

In Table 2.2, the estimated $ET_{obs,basin}$ is evaluated against observed P-R. Note that the uncertainty of the GPCP data may be of order 10% [*Fekete et al.,* 2004]. The uncertainty in the CPC data can be 6% for annual precipitation over land [*Chen et al.,* 2002]. Uncertainty in streamflow measurements can also be 6-7% based on comparison with estimates derived using satellite radar topography [*LeFavour and Alsdorf*, 2005]. The fourth column of Table 2.2 shows that annual $ET_{obs,basin}$, estimated to be 1134 mm, matches more closely (within ~4%) the annual P-R estimated from CPC precipitation data and streamflow measurements. In contrast, P-R estimated using GPCP rainfall data, is 298 mm (26%) lower than $ET_{obs,basin}$. Using the CPC rainfall data gives a closer balance for the basin-scale surface water budget than using the GPCP data. $ET_{obs,basin}$ provides an independent constraint on the biases of the different rainfall datasets. It also suggests that our approach of scaling flux tower ET probably provides a reasonable annual ET for the Amazon River basin for the period when flux tower measurements were available, although it is still possible that both precipitation and observed ET have a low bias of order 10%.

Table 2.2. Area mean surface water budget variables for ERA40 and observations. The observed ET is the annual mean, averaged over the eight tower datasets shown in Figure 2.7.

Precipitation (mm)	**Runoff/ Streamflow (mm)**	**P-R (mm)**	**ET_{basin} (mm)**	**ET_{tower} (mm)**
CPC **2179**	O+A **1087**	1092	**$ET_{obs,basin}$** **1134**	$ET_{obs,\ towers}$ 1200
GPCP 1925	O+A 1087	838		
ERA40 1973	ERA40 828	1145	$ET_{ERA40,basin}$ 1289	$ET_{ERA40,\ towers}$ 1363

2.4 Conclusions

The surface water budget variables from ERA40 over the Amazon River basin were examined on seasonal, annual and interannual scales using the available observational data to clarify the strengths and limitations of the reanalysis. The ERA40 annual precipitation is about 10% lower than that of CPC rain-gauge based dataset due to the underestimation of wet season rainfall, but agrees well with the GPCP rainfall data. However, the surface water budget analysis using independently observed streamflow and ET data suggests that GPCP underestimates rainfall. The CPC rainfall data provides a more nearly balanced surface water budget. Interannual variations of the annual rainfall, particularly the larger variations related to ENSO episodes are qualitatively represented by the reanalysis, although their amplitude is underestimated. On the sub-basin scale, ERA40 underestimates rainfall compared to the CPC data over most of the Purus-Juruá, Madeira, Solimões and Tapajós-Xingu River basins during the wet season (DJF), with some areas showing an underestimation greater than 300 mm (~30%). During the dry season (JJA), rainfall is overestimated by as much 300 mm (~40%) in parts of the Purus-Juruá and Madeira River sub-basins and underestimated by approximately the same

amount in parts of the Negro and Solimões River sub-basins, despite good agreement in the basin-mean precipitation.

The total annual runoff in ERA40 is on average 25% lower than that suggested by river flow measured at Óbidos and Altamira near the mouth of the Amazon River. ERA40 shows similar rain-rate intensities when compared with the rain-rate of spatially and temporally re-scaled TRMM data. However, even the native resolution of ERA40 is greater than the spatial scale of convective systems, so modeled rain-rates are less than those observed. There is a possibility that the model interception may have a high bias, which contributes to the high ET in the rainy season, and reduces the wet season storage.

ET in ERA40, averaged over grid-points co-located with flux tower measurements, agrees with that measured within the observational uncertainty. Individually however, in five out of nine years, ET in ERA40 is larger than that observed by more than 20%, suggesting that the ERA40 ET may have a high bias, despite the probable low bias of the eddy covariance method of order 10%. This high bias of ERA40 is seen over the entire seasonal cycle.

The observed difference between precipitation and runoff (denoted as P-R) agrees more closely with the P-R of ERA40 than with the ET of ERA40, which is augmented by soil moisture nudging. On the seasonal scale, soil moisture nudging is largest during the dry season, when it is needed to produce a more realistic ET. This addition of soil water appears to compensate for the low soil moisture recharge during the previous wet season. Insufficient recharge may be caused in part by the underestimation of rainfall during the wet season. However the relatively shallow rooting layers in the reanalysis model do not represent the deep soil water reservoir characteristic of the Amazon forest.

We propose a method to scale up in-situ ET fluxes to basin scales using the ERA40 estimated basin-averaged annual ET. This scaled ET agrees with the observed difference between precipitation and runoff, P-R, to within 4% if we use the CPC rainfall data. This approach allows us to balance the surface water budget averaged over the Amazon River basin within observational uncertainty.

Reanalyses provided by global forecast and analysis systems are often used as surrogates for studying atmospheric and surface hydrological cycle processes. However, certain applications should be viewed with caution, especially those involving long-term changes of runoff, detailed spatial distribution of rainfall and the closure of the water budget.

CHAPTER 3

THE AMAZON WET SEASON ONSET VARIABILITY AND ITS LINKAGE TO EXTRATROPICAL WEATHER SYSTEMS

3.1 Introduction

The interannual variability of the wet season precipitation, which is often due to the variability of its onset [*Liebmann and Marengo*, 2001], is an important aspect of the hydrometeorology of the Amazon. The Amazon local ecosystem and agricultural activities are most sensitive to interannual variations of the wet season onset (dry season length) than to wet season total rainfall [*Sombroek*, 2001]. The physical processes involved in the wet season onset relate to both land atmosphere interactions as well as large scale dynamics [*Fu and Li*, 2004; *Li and Fu*, 2004; *Liebmann et al.*, 2007; *Marengo et al.*, 2001]. *Marengo* [2001] finds a close relationship between the onset dates in different regions of the Amazon and sea surface temperature anomalies (SSTA), except in the southern Amazon. *Li and Fu* [2006] demonstrated a close relationship between the wet season onset in southern Amazon and incursion of cold air systems into subtropical latitudes to the east of the Andes. During the transition season, an increasingly moister and warmer atmosphere provides favorable thermodynamic conditions for a sudden increase in convection when low level wind convergence along cold fronts' leading edge lift the local warm and unstable air.

However, no study has yet investigated long term changes in the incursion of cold air systems into central South America and their potential influence on the wet season

onset in the southern Amazon. In this Chapter a delaying trend in the southern Amazon wet season onset is presented and evaluated against an observed decrease in cold air incursion (CAI) days in central South America.

3.2 Data and Methods

The European Centre for Medium-Range Weather Forecast Reanalysis (ERA40) daily temperature, mean sea level pressure (SLP) and meridional wind are used to calculate cold air incursion days. This product was obtained at the National Center for Atmospheric Research (NCAR) for the period January 1979 to August 2002 at 1.125^{o} latitude/longitude spatial resolution and 4 times daily that were then averaged to daily means [*Comeaux and Worley*, 2005]. The coarser ERA40 2.5^{o} latitude/longitude spatial resolution temperature and relative humidity was also used in the calculation of domain averaged equivalent potential temperature (θe) at 925hPa and saturation equivalent potential temperature (θes) at 850hPa.

Studies characterizing the incursion of cold air into South America, often evaluate intensity and/or frequency of events averaged over a pre-defined domain in the subtropics [*Garreaud*, 2000; *Li and Fu*, 2006]. In winter the occurrence of intense frost events in a pre-defined area of interest, can also be used as a criterion for defining an anomalously active winter [*Muller et al.*, 2005; *Muller and Ambrizzi*, 2007]. The spatial distribution of cold air incursions cannot be clearly obtained using these criteria. Therefore I propose a method following *Cavalcanti and Kousky* [2003] and described as follow: at each grid cell in South America and adjacent oceans, a surface temperature drop of at least 2^{o}C, sea level pressure (SLP) increase of at least 2hPa in 24 hours, and southerly winds of at least 2 m/s must be observed. I applied the aforementioned criteria for each transition season

consisting of the months of September, October and November (SON). The total number of days satisfying the set of criteria is defined and counted at each grid point in South America and adjacent oceans.

The wet season onset follows *Li and Fu* [2004] and is defined as the pentad in which the average rainrate (in mm/day) changes from below the long-term annual average in six out of eight pentads before this date to above the annual mean in the six out of eight pentads after this date in the southern Amazon domain (15°S-5°S and 70°W-50°W). An improved gridded daily precipitation dataset developed at the National Oceanic and Atmospheric Administration (NOAA) - Climate Prediction Center (CPC) is used in this study [*Silva et al.*, 2007], henceforth referred to as CPC_{daily}. Although ERA40 data is used for most calculations, the precipitation spatial distribution in the reanalysis does not agree well with observations in the Amazon [*Fernandes et al.*, 2008], hence the choice to use the gauge only CPC_{daily}. CPC_{daily} covers the period from January 1978 to August 2006 and the entire timeseries is used in the calculation of the wet season onset, but trend analysis was also performed for the subset period of 1979-2001 to match the analysis period of ERA40. The calculations involving ERA40 are restricted to 1979-2001 to match the beginning of satellite data assimilation into ERA40 to the last transition season available. The trends calculated are done using the non-parametrical and outliers resistant Mann-Kendall trend test [*Kendall*, 1938; *Mann*, 1945] and Sen's slope [*Sen*, 1968]. The significance of correlations throughout the document is tested using a two-tailed t-test [*Wilks*, 2006].

3.3 Results

The southern Amazon wet season onset pentads for the period 1978-2006 are presented in Figure 3.1. A delay in the wet season onset is seen from the late 1970s towards the early 2000s, describing a positive trend of about 2 pentads per season per decade significant at the 99% level. For the period 1979-2001 the trend is about 1.3 pentad per season per decade significant at the 90% level.

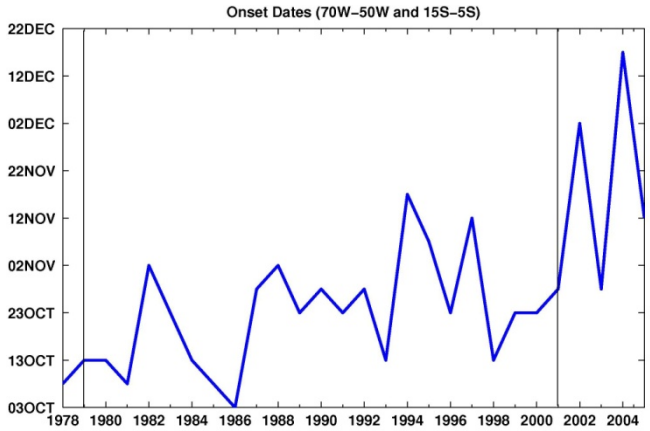

Figure 3.1.Timeseries of southern Amazon (15°S-5°S and 70°W-50°W) wet season onset pentad. The dates on the y-axis represent the first day of the pentad. The vertical lines mark the period for which CAI days were calculated.

A delayed wet season onset may be related to unfavorable land surface and atmospheric thermodynamic conditions and/or an inactive CAI events season [*Li and Fu*, 2006]. Cold fronts are the most common synoptic weather systems in South America, causing most of the precipitation observed in the subtropical and extratropical latitudes [*Cavalcanti and Kousky*, 2003]. Cold fronts moving over the Bolivian Plateau, enhance low-level moisture convergence and can trigger convection at low latitudes [*Garreaud*, 1999; *Oliveira*, 1986]. Frequent cold air incursions reach southern Amazon during the

transition season (September and October) as the atmosphere in central Brazil becomes destabilized. The resultant precipitation not only increases the soil moisture and latent heat fluxes but also effectively convert the potential energy accumulated near the surface into rotational kinetic energy, which spins up the anticyclonic circulation in the upper troposphere. The reoccurring cold air events play an important role in driving the circulation transition from dry to wet season [*Li and Fu*, 2004; *Raia and Cavalcanti*, 2008]. Therefore, changes in CAI days in South America are likely to have an impact on the wet season onset in southern Amazon.

A 23 years composite of precipitation, sea level pressure (SLP) and temperature difference between the onset and previous and subsequent pentads, respectively are shown in Figure 3.2. Along with the sharp increase in precipitation in southern Amazon during the onset compared to the previous pentad, an area of lower temperature and higher SLP are observed in central South America, consistent with a cold air mass moving towards central Brazil (Figure 3.2 a, b, c). Another characteristic of a cold front passage is the center of low pressure over the southern coast of Brazil seen during the onset (Figure 3.2 b). During the following pentad precipitation reduces slightly compared to that occurred during the onset pentad over much of the southern Amazon, but is sustained or slightly increased to the east and north of the southern Amazon domain, whereas an increase in temperature and decrease in SLP is observed in central South America (Figure 3.2 d, e, f).

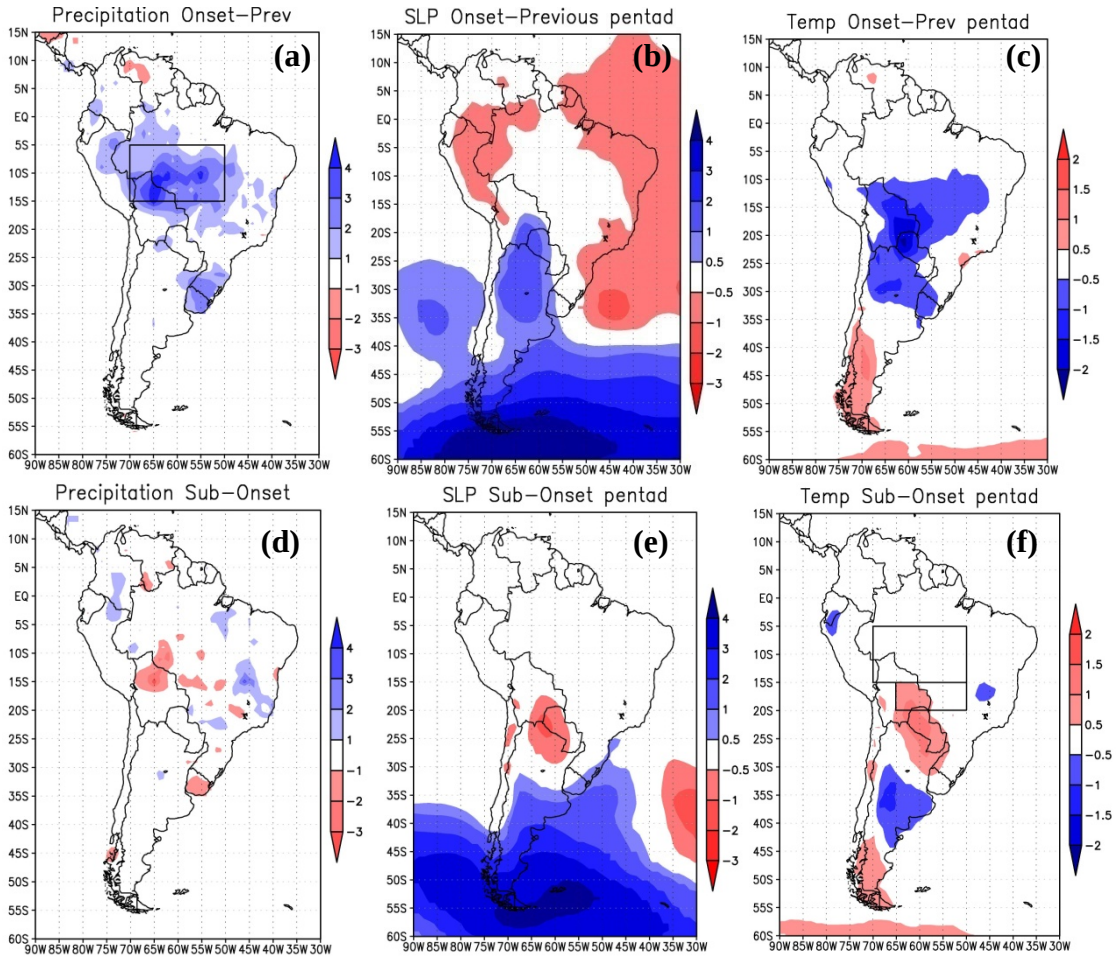

Figure 3.2. Precipitation (mm/day), mean sea level pressure (hPa) and temperature (^{o}C) difference between the onset and previous pentads (a), (b) and (c) and subsequent and onset pentads (d), (e) and (f). The domain for which the onset was calculated is shown in (a), whereas in (f) the domains in which significant CAI is evaluated is shown.

Although the composites shown in Figure 3.2 suggest an atmospheric pattern characteristic of a cold air mass displacement over South America, not every individual season had a CAI associated with the onset. From the 23 years (1979-2001) for which the CAI days were calculated, 15 years (65%) had one significant cold air incursion event during the onset or within one pentad from the onset as shown in Table 3.1.

Table 3.1. Wet season onset pentads and dates for the period 1979-2001. Significant cold air incursion (CAI) events that occurred during the (or within one) pentad of the onset are also listed.

Year	Onset Pentad	Pentad's first day	CAI		Year	Onset Pentad	Pentad's first day	CAI
1979	58	13-Oct	15-Oct		1991	60	23-Oct	
1980	58	13-Oct	13-Oct		1992	61	28-Oct	29-Oct
1981	57	8-Oct	14-Oct		1993	58	13-Oct	
1982	62	2-Nov	4-Nov		1994	65	17-Nov	
1983	60	23-Oct	24-Oct		1995	63	7-Nov	
1984	58	13-Oct			1996	60	23-Oct	21-Oct
1985	57	8-Oct	8-Oct		1997	64	12-Nov	15-Nov
1986	56	3-Oct	8-Oct		1998	58	13-Oct	
1987	61	28-Oct	27-Oct		1999	60	23-Oct	22-Oct
1988	62	2-Nov	2-Nov		2000	60	23-Oct	28-Oct
1989	60	23-Oct	27-Oct		2001	61	28-Oct	30-Oct
1990	61	28-Oct						

Two spatial domains are considered in determining a significant cold air event. The northern domain (15^{o}S-5^{o}S and 70^{o}W-50^{o}W, the northern box in Figure 3.2f), or the main domain, captures the usual spread of cold air masses that move well into subtropical South America during the onset (see Figure 3.2c), and is the same domain chosen to calculate the onset pentads. The southern domain (20^{o}S-15^{o}S and 65^{o}W-50^{o}W, southern box in Figure 3.2f), or the second domain, is also considered to capture CAI occurred

slightly to the south of the main domain in case no significant cold air event is identified in the northern domain. A significant cold air event is defined according to the following steps: i) the number of cells that obey the criteria of CAI within the northern domain is counted and must be at the upper one third of the most extensive CAI events for that domain and month; ii) if the number of cells that obey the criteria of CAI is not significant as per criterion (i), the same analysis is done considering the southern domain.

Figure 3.3 shows the number of cold air events as a function of numbers of gridcells it spreads over for each transition season month and CAI domain. The total number of events is determined by pooling the number of cells for every day that had at least one cell obeying the criteria of CAI in each domain. In the northern domain, the 30% most extensive cold air masses cover 18, 10 and 13 gridcells corresponding to 12%, 6% and 8% of the total area in September, October and November, respectively. In the southern domain the 30% most extensive cold air masses cover 27, 13 and 10 gridcells corresponding to 45%, 22% and 17% of the domain area in the same three months, respectively. For example, in 1979 the CAI event of October 15th (Table 3.1) that occurred during the onset pentad, spread over 37 cells (23% of the domain area) in the northern domain, which is in the upper 30% threshold for significance in October (10 gridcells) (Figure 3.3 c). The above mentioned fractional area for each month and domain is used as the threshold to determine whether a CAI event is significant or not for that month and domain. When a pentad that include days in 2 different months, for example, September 28th to October 2nd, the threshold to determine whether or not a CAI event is significant is the average number of the two thresholds for September and October in the domain of interest.

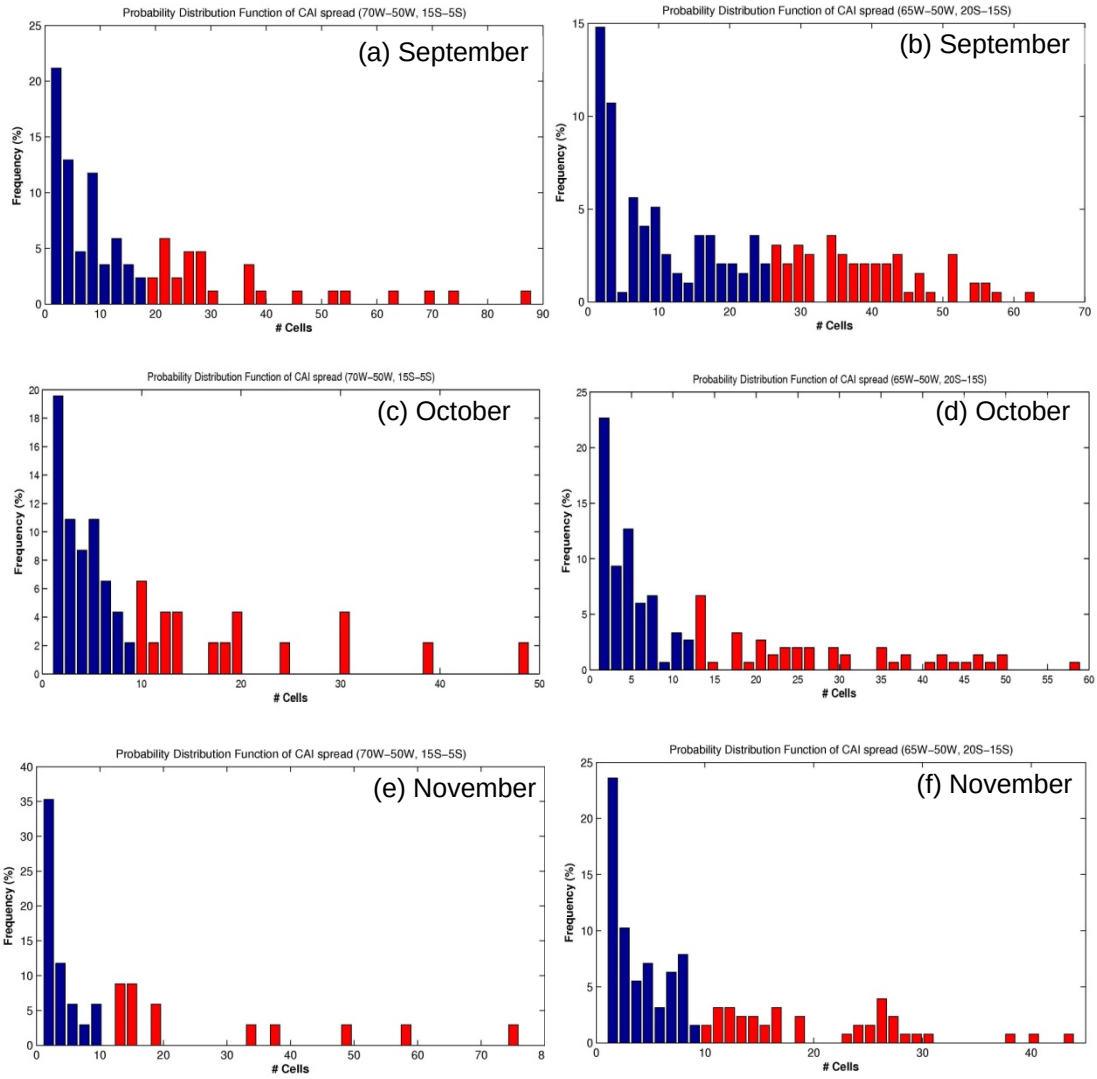

Figure 3.3. Number of cold air events as a function of spread area (number of gridcells) that obey the criteria for CAI in the domains 15°S-5°S and 70°W-50°W (left hand side) and 20°S-15°S and 65°W-50°W (right hand side) in September (a) and (b), October (c) and (d) and November (e) and (f). The red bars represent the upper 30% most extensive events.

The spatial distribution of climatological CAI days in South America during SON is shown in Figure 3.4. Extratropical transient systems moving along the subtropical jet stream, tend to cross the Andes at latitudes of 35°S to 45°S [*Cavalcanti and Kousky*, 2003], then most assume a northward displacement channeled by the Andes toward Paraguay. These systems define a path in which the highest number of days under CAI influence is observed in SON, averaging 14 and above days per season (Figure 3.4).

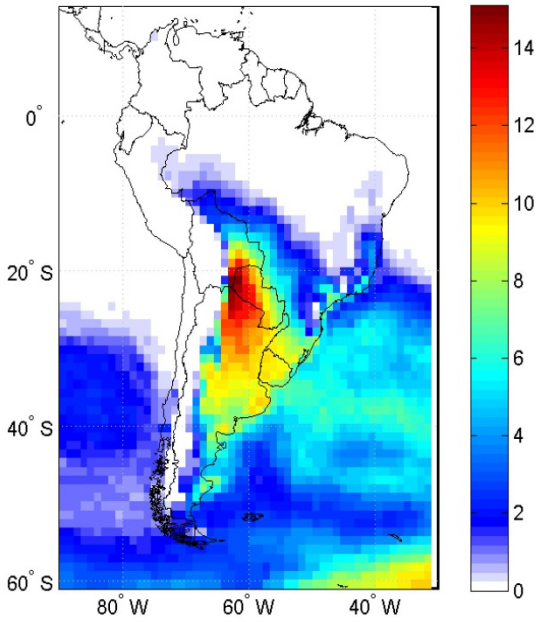

Figure 3.4. SON average number of CAI days in South America for the period 1979-2001.

A seasonal relationship between the wet season onset and CAI in the southern Amazon is shown in Figure 3.5, in the form of a CAI index calculated by averaging the seasonal CAI days in the main domain (15°S-5°S and 70°W-50°W) and plotted against the wet season onset pentad. The correlation between the number of CAI days and the time of the onset is -0.45, significant at the 95% level, indicating that early (late) onset is

favored in years in which greater (lower) frequency of CAI events occurs in the southern Amazon (Figure 3.5).

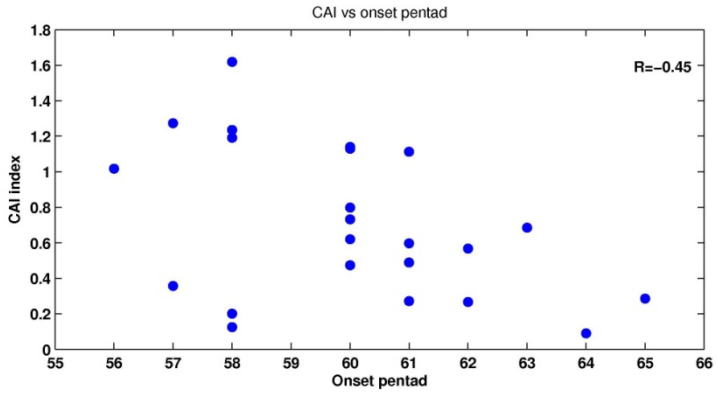

Figure 3.5. Domain averaged and (15°S-5°S and 70°W-50°W) CAI days in SON and onset pentads.

This relationship can be further explored by evaluating the seasons in which the onset was early and late by more than 2 pentads of its normal date, which is pentad 60 or the pentad starting in October 23rd. The years 1981, 1985 and 1986 registered an early wet season onset, whereas in 1994, 1995 and 1997 the onset was late by more the 2 pentads (Table 3.1). The daily number of cells that obey the criteria for CAI in the domain 20°S-15°S and 65°W-50°W are shown for the early and late onsets (Figure 3.6 a and b). During the early onset years, CAI events are noticed as early as the first week of September, re-occurring every ten days or so into early October until the onset is established (pentads starting on October 3rd and 8th, marked with arrows in Figure 3.6a). During the late onset, CAI events are also observed but they are less frequent early in the season (Figure 3.6b) when compared to those occurring in years of early onset. Additionally, during the late onset only a few events reach the threshold required to

define them as significant in the domain 20^{o}S-15^{o}S and 65^{o}W-50^{o}W, marked as a horizontal black line in Figure 3.6a and Figure 3.6b. The results discussed above are insensitive to the choice of domain and lower (higher) frequency of CAI events is also found during late (early) onset in the northern domain (not shown).

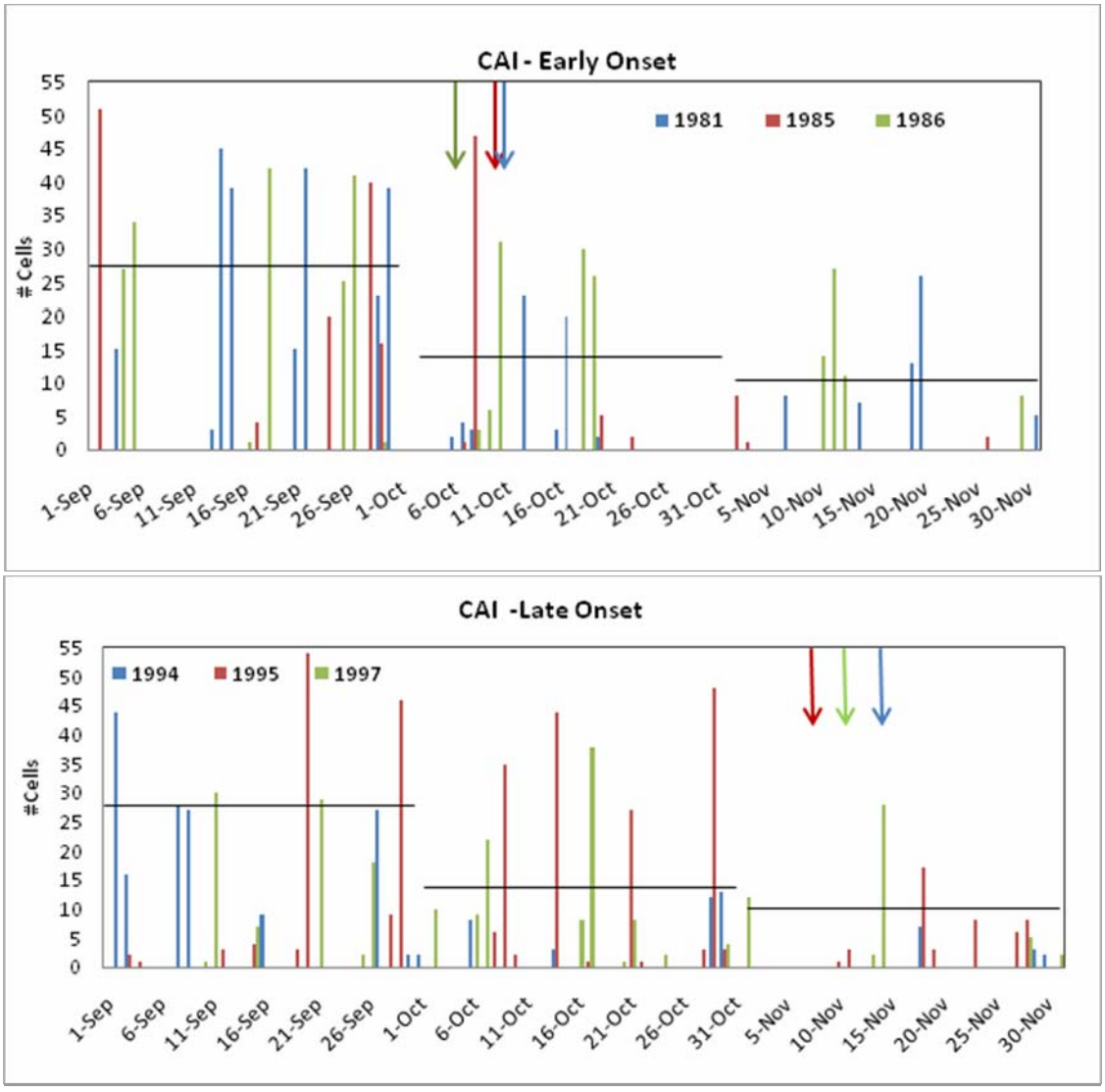

Figure 3.6. Daily CAI events for (a) early and (b) late onset seasons. The scale on the y-axis represents the total of cells over which a CAI event spread in the domain 20°S-15°S and 65°W-50°W. The arrows represent the wet season onset for the years labeled.

As shown in the work of *Li and Fu* [2004] and *Fu and Li* [2004], the wet season onset is also closely related to land surface thermodynamic conditions. The authors have shown that previous to the onset, an increase in latent heat flux works as to destabilize the boundary layer leading to convection in the region. The combined effect of land surface processes and extratropical influence ultimately determine the characteristics of the wet season onset. The results presented in this study suggest that an early Amazon wet season onset is influenced by a regular income of intense CAI events early in the season into southern Amazon. In order to assess the time evolution of the background thermodynamics during the early and late onset, the difference between the equivalent potential temperature (θ_e) at 925hPa and the saturation equivalent potential temperature (θ_{es}) at 850hPa ($\theta_{e,925hPa}$- $\theta_{es,850hPa}$) for the early and late onset composites is examined as an approximate indicator of the convective inhibition energy (CINE) for the southern Amazon domain (15°S-5°S and 70°W-50°W). The θ_e at 925hPa is an indicator of buoyancy of the air in the surface layer, whereas θ_{es} at 850hPa indicates the minimum buoyancy that is required for an air mass to rise spontaneously if it were lifted to 850hPa. Thus, $\theta_{e,925hPa}$- $\theta_{es,850hPa}$ represents the work needed to lift an air parcel from 925hPa to 850hPa. The equivalent potential temperature (θ_e) and saturation equivalent potential temperature θ_{es} equations are shown below:

$$\theta_e \cong \left(T + \frac{L_v}{c_p} w \right) \left(\frac{p_o}{p} \right)^{\frac{R}{cp}} \tag{2}$$

$$\theta_{es} \cong \theta \exp \left(\frac{L_v w_s}{c_p T} \right) \tag{3}$$

where - T is temperature of air at pressure p

- Lv - latent heat of evaporation (~ 2500 kJ/kg)

- w- mixing ratio of water vapor in air

- c_p - specific heat of dry air at constant pressure (1004 J/(kg K))

- p_o - standard reference pressure in hPa

- p - pressure in hPa

- R - specific gas constant for dry air (287 J/(kg K))

- θ - is potential temperature

- w_s- saturation mixing ratio of water vapor in air

Figure 3.7 indicates that the lower troposphere during earlier wet season onsets tend to be less stable thermodynamically compared to the late wet season onsets. Such a difference in instabilities indicates favorable thermodynamics conditions for frequent CAI events in September to produce large-scale increase of rainfall, and consequently accelerate the destabilization of the deep troposphere and circulation transition to wet season [*Li and Fu*, 2004; 2006].

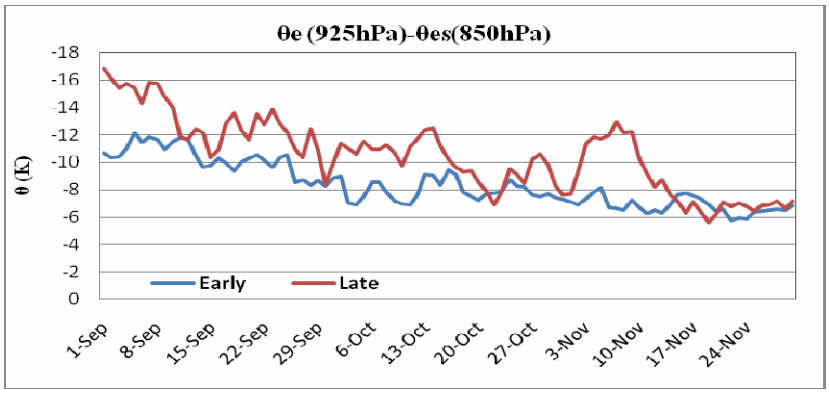

Figure 3.7. Time evolution of the difference between 925hPa θ_e and 850hPa θ_{es} for the early and late wet season onset composites averaged over the domain (15°S-5°S and 70°W-50°W). Unit (K).

To further explore the relative importance of the thermodynamics conditions and the dynamic influence of cold air incursion the southern Amazon on the wet season onset timing, the onset pentads are evaluated against domain averaged CAI index (as in Figure 3.5) and $\theta_{e,925hPa}$- $\theta_{es,850hPa}$.

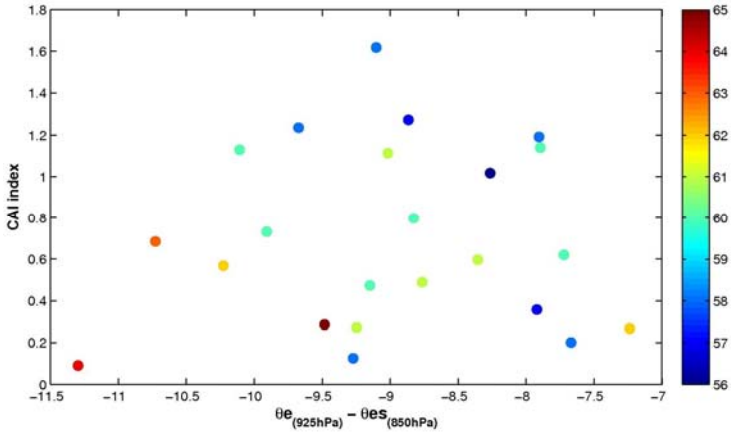

Figure 3.8. SON domain averaged CAI index (days) and $\theta_{e,925hPa}$- $\theta_{es,850hPa}$ (K). The colorbar represents the onset pentads for the period 1979-2001.

Later onsets tend to occur when both the thermodynamic and dynamic condition are weak (Figure 3.8), occurring when lower CAI index and $\theta_{e925hPa}$- $\theta_{es850hPa}$ values are observed. Earlier onsets seem to be favored in years in which we observe more CAI days and more unstable lower atmosphere (higher values of $\theta_{e925hPa}$- $\theta_{es850hPa)}$. Normal years (pentads 59-61) tend to concentrate in the middle of the plot. Noteworthy is the fact that no late onset (orange and red shades) is observed when the CAI index is above average (0.8 days averaged over the southern Amazon domain). Early onsets seem to respond to greater CAI as well as favorable thermodynamics.

The results discussed are consistent with the assumption that more frequent and widespread CAI events provide southern Amazon with the triggering mechanism that will eventually favor the earlier wet season onset. Consequently, long term changes in occurrence of CAI in southern Amazon are likely to affect the timing of the wet season onset. Since 1979, a 90% significant negative trend of around 2 days per decade per season in number of CAI days has been observed in central South America (Figure 3.9d). A decrease of a couple of days per season actually corresponds to a reduction of 30-50% of CAI days in southern Amazon, since the climatology shows values around 4 to 6 days per season (Figure 3.4). The seasonal trend (Figure 3.9d) is mostly determined by a decreasing trend in September (Figure 3.9a), when the frequency and intensity of CAI events are most relevant in determining the early southern Amazon wet season onset.

The observed reduced occurrence of CAI days in central South America is consistent with the observed delayed wet season onset, suggesting again the important role of the extratropical weather systems to tropical wet season onset. In addition the strongest long term decrease in CAI days occurs in September, when the regular incursion of cold air mass into southern Amazon favors early and normal onsets.

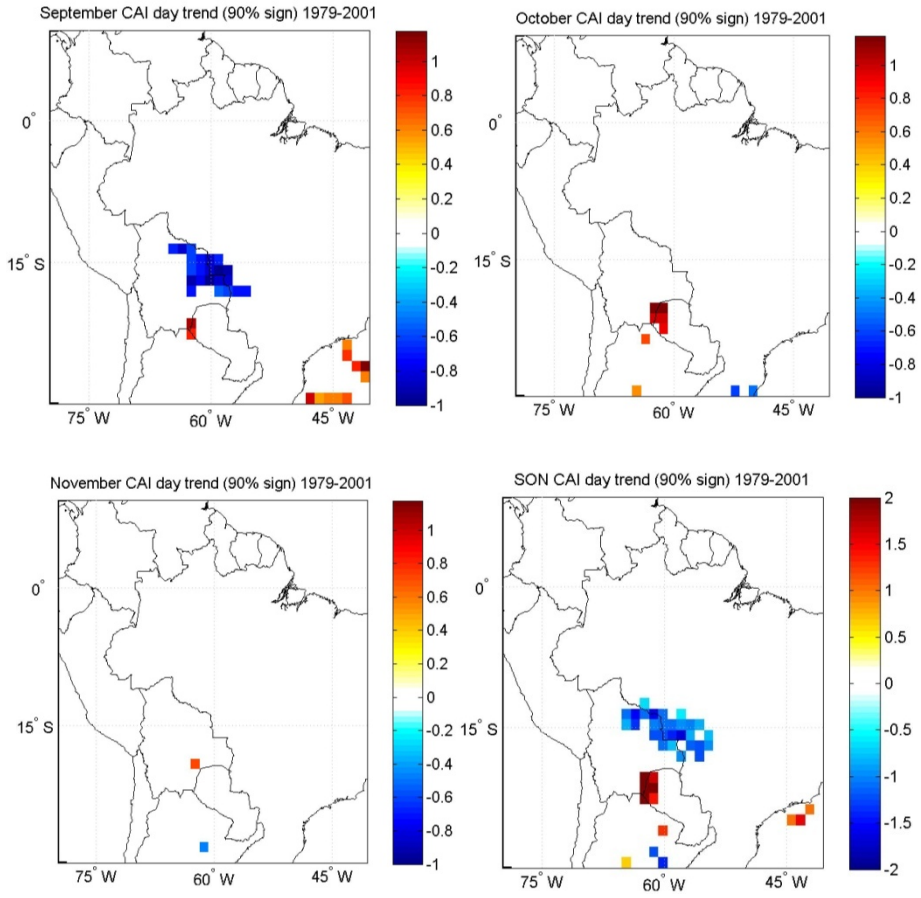

Figure 3.9. Cold air incursion days trend during (a) September, (b) October, (c) November and (d) SON 1979-2001. The colored grids are significant trends at 90% confidence level in number of days per season per decade.

3.4 Discussion and Conclusions

The southern Amazon wet season onset is determined by a combination of land surface and atmospheric thermodynamics and large scale dynamic phenomena, especially incursions of cold air into the region.

The interannual variability of cold air incursion into southern Amazon during the transition season plays an important role in determining the onset timing. In years in which early onset (early October) is observed, widespread incursion of cold air throughout the previous month occurs regularly in southern Amazon. During late onset seasons, cold air incursions do also occur but tend to be weaker and start to happen later in September.

The relative importance of the atmospheric thermodynamics and CAI on the wet season onset is evaluated in terms of the convective inhibition energy (CINE), approximated by $\theta_{e,925hPa}$-$\theta_{es,850hPa}$, and CAI days against the onset timing. Late onsets preferably occur when the lower troposphere is anomalously stable and low occurrence of CAI events is observed. Even when the thermodynamic conditions are favorable, late onsets do not occur when CAI days are above average. Hence, the occurrence of frequent and widespread CAI events during SON, especially early in the season seems to be important to prevent a late wet season onset. In addition an observed decreasing trend in CAI days is consistent with a delayed wet season onset since the late 1970s in southern Amazon.

CHAPTER 4

LARGE SCALE TELECONNECTIONS LINKED TO COLD AIR INCURSION IN SOUTH AMERICA

4.1 Introduction

The climate of South America responds to remote influences at various timescales. The El Niño Southern Oscillation (ENSO) is the main mode of variability on interannual timescales. The influence of Pacific SST anomalies, are carried by an eastward (westward) shift of the Walker Cell and by enhancement of the subtropical jet stream crossing South America, result of a sharper meridional temperature gradient in the Pacific basin [*Grimm et al.*, 1998; *Hastenrath*, 1990; *Kousky et al.*, 1984; *Ropelewski and Halpert*, 1987]. ENSO events are not always alike varying according to the timing, area and intensity the anomalous SST anomalies, and so do the atmospheric responses to the anomalous SST in the tropical Pacific [*Kidson et al.*, 2002; *Kumar et al.*, 2006; *Vera et al.*, 2004], which results in distinct planetary Rossby wave trains known as the Pacific South American modes (PSA) [*Karoly*, 1989; *Kidson*, 1999; *Mo and Paegle*, 2001].

SST anomalies in the tropical Indian Ocean and associated global teleconnections have also been given greater attention recently in literature. The Indian Ocean Dipole (IOD) [*Saji et al.*, 1999; *Webster et al.*, 1999] positive phase is linked to positive temperature anomalies to the north of 30^{o}S and positive rainfall anomalies to the south of 20^{o}S during SON in South America [*Chan et al.*, 2008; *Liu et al.*, 2007; *Saji and Yamagata*, 2003; *Saji et al.*, 2005].

On interdecadal timescales, the Pacific Decadal Oscillation (PDO) and North Atlantic Oscillation (NAO) are suggested to influence the decadal variability of South American climate, although the mechanisms for such connectivity are not clear [*Agosta and Compagnucci*, 2008; *Chen et al.*, 2001; *Garreaud and Battisti*, 1999; *Marengo*, 2004; *Paegle and Mo*, 2002]. For example, *Kayano and Andreoli* [2007] find that positive PDO (cold northern and warm central-tropical Pacific) enhances the effect of El Niño in South America, whereas *Mestas-Nuñez and Miller* [2006] find the low frequency ENSO-like (closely related to PDO) pattern of upper level divergence over northern South America to be the opposite of same phase ENSO during austral summer.

In studies of Amazon precipitation variability, SST anomalies are shown to be connected to both total accumulated amounts [*Chan et al.*, 2008; *Grimm et al.*, 1998; *Hastenrath*, 1990; *Haylock et al.*, 2006; *Marengo*, 2004] and wet season onset timing [*Fu et al.*, 1999; *Liebmann and Marengo*, 2001; *Wang and Fu*, 2002] in the northern Amazon. In the southern Amazon however, *Marengo* [2001] shows no significant relationship between the onset and SST variability.

In this Chapter we present evidence that the SST effect on the southern Amazon wet season onset is mainly related to its impact on extratropical incursion of cold air during the transition season.

4.2 Data and Methods

Cold air incursion (CAI) days are calculated for each season (SON) and each grid cell as described in Section 3.2, using the higher spatial resolution (1.125^o latitude by 1.125^o longitude) ERA40 data. The monthly HadSST2 (1^o latitude by 1^o longitude) dataset described in *Rayner et al.* [2006] is used to compute SON SST means and

anomalies for the base period of 1979-2001, matching the time period available in ERA40. Upper atmosphere winds and derived variables presented in sections 4.2.1 to 4.2.3 was performed using the coarser ERA40 (2.5^{o} lat x 2.5^{o} lon), whenever the domain exceeds the Southern Hemisphere, otherwise the finer resolution ERA40 is used.

The main modes of co-variability between CAI and sea surface temperature (SST) are evaluated by performing a Singular Value Decomposition (SVD) analysis [*Bretherton et al.*, 1992] of the SON CAI days and SST anomalies covariance matrix. The SVD of a cross-covariance matrix yields two spatially orthogonal sets of singular vectors and a set of singular values associated with each pair of vectors, also called expansion coefficients (EC) [*Bjornsson and Venegas*, 1997]. An EC pair (one for each variable) describes how each SVD mode progresses in time; henceforth following the notation indicating their respective variable and mode (examples: SST-EC1, CAI-EC2). Each pair of spatial patterns describes the squared co-variance fraction (SCF) between the two variables and is presented in the text in terms of percentage of total co-variance.

Three modes of CAI days and SST co-variability are presented in the next sections and they account for 73% of the total co-variability between these the 2 fields. The spatial patterns corresponding to different SVD modes are shown as homogeneous (heterogeneous) correlation maps, which is the correlation between the n-th mode's EC and the values of the same (other) field at each gridpoint. The SVD analysis is performed to examine the co-variability of CAI days in southern Amazon where significant decadal changes are observed (Figure 3.9d) and global SST, thus the CAI days domain used in the analysis is 30^{o}S-10^{o}S and 70^{o}W-50^{o}W. The usage of global SST eliminates any spatial bias as to which oceanic region impacts CAI days. Finally, the strength of the

coupling between CAI days and SST anomalies in each mode is presented as correlation between the fields' ECs.

To further evaluate whether any of the three modes discussed in this chapter are related to the CAI days trends presented in Section 3.3, the series is reconstructed for each of the three modes and then a trend analysis is performed in the reconstructed series. The reconstruction of the CAI days series is presented below in its general form.

$$CAI_{t,x} = \sum_{i=1}^{N} EC_i(t)\, EOF_i(x) \tag{4}$$

where – *EC* is i-th mode expansion coefficient

- *EOF* is the standing spatial pattern of the i-th mode.

- *(t)* and *(x)* corresponds to the time the space domains respectively used in the analysis

The results are presented in three sections 4.2.1, 4.2.2 and 4.2.3 describing respectively the first, second and third mode of co-variability between SST and CAI days. The resulting paired variability is further analyzed as to determine some key atmospheric characteristics explaining the connection between SST and CAI days anomalies. The method employed involves compositing the variables during the seasons that are above (+1) and below (-1) standard deviation with respect to each mode's SST-EC then calculating the difference between the composites. The first and second modes are briefly described as to characterize the large scale mechanisms responsible for the respective response in the CAI days variability in South America, whereas the third mode is given more attention since it reproduces the CAI days trend almost in its entirety.

4.3 Results

4.3.1 First Mode of co-variability between SST and CAI days (SVD1)

The first mode of co-variability between CAI days and SST anomalies is shown in Figure 4.1 in the form of homogeneous and heterogeneous correlation spatial patterns, which were colored to intuitively represent negative (positive) field anomalies as negative (positive) correlations. Heterogeneous correlation tend to be lower than homogeneous correlation thus the significance shown (two tailed t-test) are at the 90% and 95% levels respectively. The co-variability between SST and CAI days indicate that positive (negative) SST anomalies in the central-tropical Pacific relate to negative (positive) anomalies in the number of CAI days in central South America, defined as the domain used in the SVD analysis (box in Figure 4.1b). Warmer central and colder western tropical Pacific are regions of greater influence in CAI days variability shown as heterogeneous correlation between CAI days-EC and SST (Figure 4.1c and d). The tropical north Atlantic also appears as an area of significant correlation in the heterogenous map, although in an area not previously reported to influence the displacement of transients reaching South America. This mode of co-variability explains 34% of the squared covariance factor of these two fields and 24% of CAI variance in the domain 30^{o}S-10^{o}S and 70^{o}W-50^{o}W.

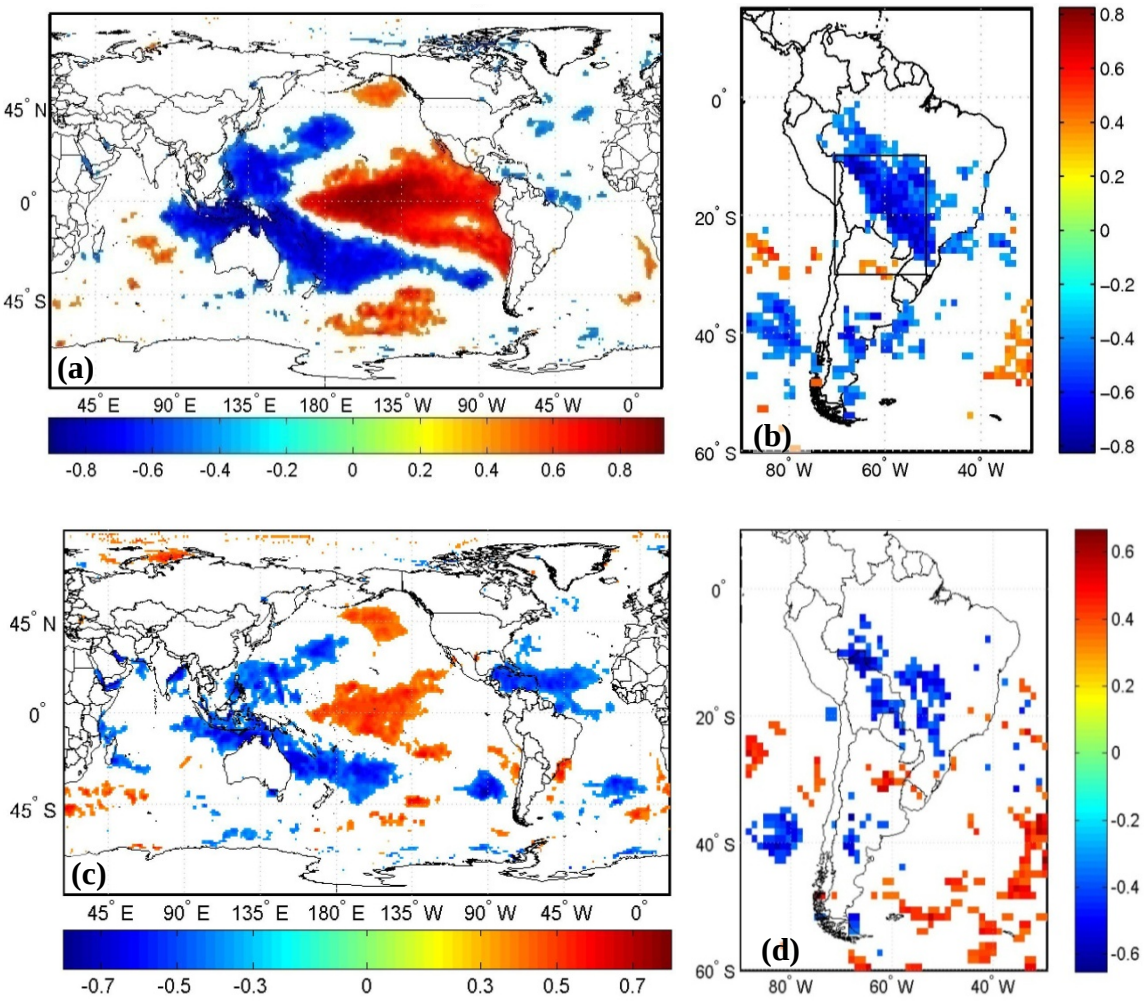

Figure 4.1. SON SVD1 homogeneous correlation maps of (a) global SST anomalies and (b) CAI days. SST anomalies (c) and CAI (d) heterogeneous correlation maps. Shaded areas are 95% significant correlation in (a) and (b) and 90% significant correlation in (c) and (d).

The correlation spatial patterns indicate the familiar SST anomalies distribution associated with ENSO. SST-EC1 is highly correlated (R=0.9) with the Oceanic Niño Index (ONI), indicating that not only the spatial distribution of SVD1 SST anomalies are related to ENSO but the interannual variability is related to that of ENSO as well (Figure 4.2 b). ONI is a three months running mean of anomalies in the Niño 3.4 region (5°N-5°S, 120°-170°W), based on the 1971-2000 base period [*CPC*, 2009]. The strength of this mode's coupling is shown in Figure 4.2 a, indicating a 95% significant correlation of 0.69 between SST-EC1 and CAI-EC1.

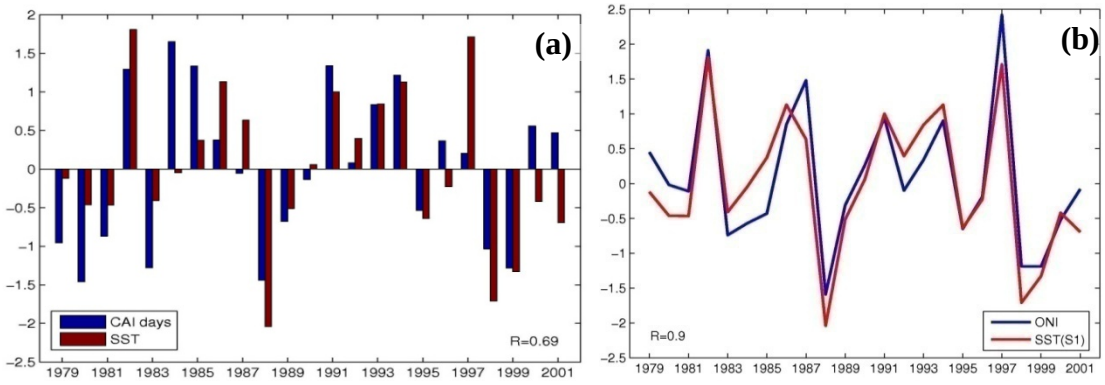

Figure 4.2 SST-EC1 and CAI-EC1 time series for the first mode of co-variability (a). Oceanic Niño Index (ONI) (°C) and SST-EC1 timeseries (b). The expansion coefficients are normalized by their respective standard deviations and are dimensionless.

One effect of El Niño is the strengthening of the subtropical jet stream, the result of a sharper meridional temperature gradient in the Pacific basin [*Ropelewski and Halpert*, 1987]. Transient waves propagate along the upper troposphere jet streams being those of interest to South American climate the subtropical and subpolar jet stream over the Pacific Ocean [*Ambrizzi et al.*, 1995; *Berbery and Vera*, 1996; *Muller and Ambrizzi*,

2007; *Pezza et al.*, 2007]. Most studies however concentrate on the impact of the jet streams variability associated with ENSO during the austral winter (JJA) or summer (DJF) months. Thus, in order to assess the mechanisms connecting ENSO and CAI days in South America during SON, composite differences for the 250hPa zonal wind, storm track activity (v'^2) and geopotential height are presented. The composites difference is determined by the averaged values for a given variable for the years above one standard deviation ($+1\sigma$) of SST-EC timeseries minus that for years below -1σ (Figure 4.2a). For simplicity the differences will be referred to as warm minus cold, which in the case of SVD1 relates to El Niño-La Niña. In other words, the composite differences presented here depict an enhanced El Niño whereas La Niña would have the opposite sign.

The stronger subtropical jet stream over the central-eastern Pacific Ocean typical of El Niño years, is seen in Figure 4.3a, extending from eastern Australia to South America around the latitude of 30°S. The storm track activity (v'^2) (Figure 4.3b) indicate a preferential band of wave propagation (positive values) in the subtropical Pacific between latitudes of 20°S and 30°S, which upon reaching South America seem to be deflected southward over central Argentina, following the subtropical jet stream. Another band of high activity is found along the subpolar jet at latitudes of 70°S. Storm track activity is defined as the 24-h difference-filtered 250-hPa meridional velocity variance v'^2 as in Equation 5 [*Chang*, 2004; *Wallace et al.*, 1988]. The overbar in Equation 5 represents seasonal means.

$$v'^2 = \overline{[v(t+24h) - v(t)]^2} \tag{5}$$

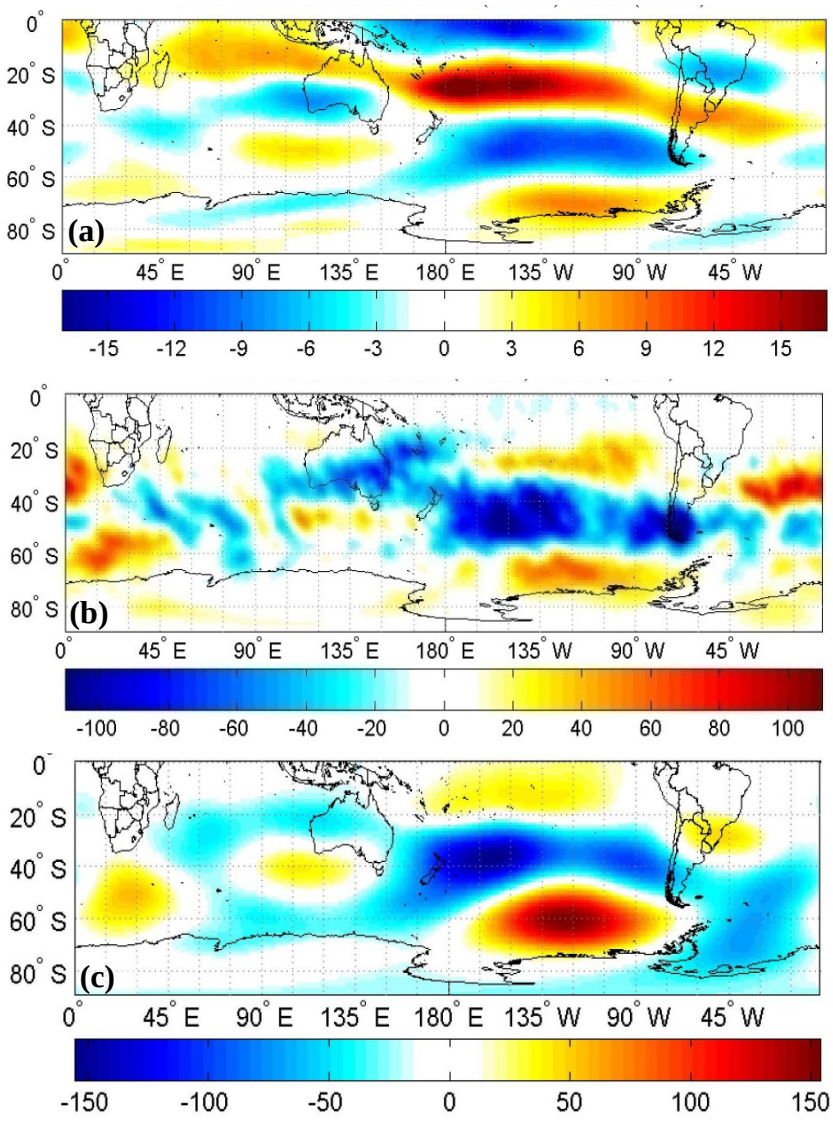

Figure 4.3. SON difference between composites in which SST-EC1 is above and below one standard deviation for 250 hPa (a) Zonal wind (U), (b) Storm track activity (v'^2) and (c) Geopotential height (Z). Units: U (m/s), v'^2(m^2/s^2) and Z (m).

This behavior is consistent with lower occurrence of SON CAI days in central South America during El Niño years, when the southward deflected subtropical jet stream over South America "guides" the transients southward as well. To the south, the subpolar jet works as a waveguide to transients at high latitudes. These two banded waveguides reflect a lower incidence of wave propagation around the latitude of 35°S-45°S where typically transients that eventually reach the continent's tropics and subtropics cross the Andes [*Cavalcanti and Kousky*, 2003; *Vera and Vigliarolo*, 2000]. This behavior is consistent with previous studies showing greater probability of occurrence generalized frost events in central South America during La Niña years than during normal or El Niño years [*Muller et al.*, 2005; *Muller and Ambrizzi*, 2007; *Vera et al.*, 2004; *Vera and Vigliarolo*, 2000].

The 250hPa geopotential height composite differences (Figure 4.3c) show an area of strong positive anomalies in the southern Pacific to the southwest of South America, describing a tendency for more persistent blocking events [*Diaz et al.*, 1998; *Mo and Paegle*, 2001; *Renwick and Revell*, 1999], which is consistent with the negative anomalies in CAI days in central South America during El Niño years. This area of geopotential height anomalies is the result of a wave train extending from tropical Pacific to South America, characteristic of the Pacific South American (PSA1) mode, regarded as the atmospheric response to the low frequency (48 months) ENSO cycle [*Kidson*, 1999; *Mo*, 2000; *Mo and Paegle*, 2001]. PSA1 will be further discussed in section 4.2.3, when the SVD3 features are compared to SVD1.

The atmospheric patterns related to this mode's SST anomalies spatial distribution reveal that a stronger subtropical and subpolar jet streams along with an atmospheric

blocking feature in the southern Pacific are unfavorable to the incursion of cold air masses into central South America during El Niño years (opposite behavior during La Niña).

In this section ENSO influence is shown to affect the frequency and spatial distribution of CAI in South American subtropics during SON. SVD1 explains mostly interanual variance in CAI days. No trend results from CAI days reconstructed from this mode in central South America.

4.3.2 Second Mode of Co-variability between SST and CAI days (SVD2)

The second mode of co-variability between SST and CAI days accounts for 22% of the total squared covariance between these two fields and 11% of the variance in CAI in the domain 30°S-10°S and 70°W-50°W. SVD2 features positive anomalies in the eastern Pacific SST and northern Atlantic as well as warm (cooler) waters in the western (eastern) tropical Indian Ocean (Figure 4.4a). The resulting coupling appears to relate to positive CAI days anomalies outside our southern Amazon domain (15°S-5°S 70°W-50°W) over Paraguay (Figure 4.4b) and off southern Brazil's coast. The heterogeneous correlation between the time series of the SST and CAI days (Figure 4.4c and d) confirms that more CAI days in central South America in SON is correlated with warmer SSTs in the eastern tropical Pacific, the western Indian Ocean and the northern tropical Atlantic.

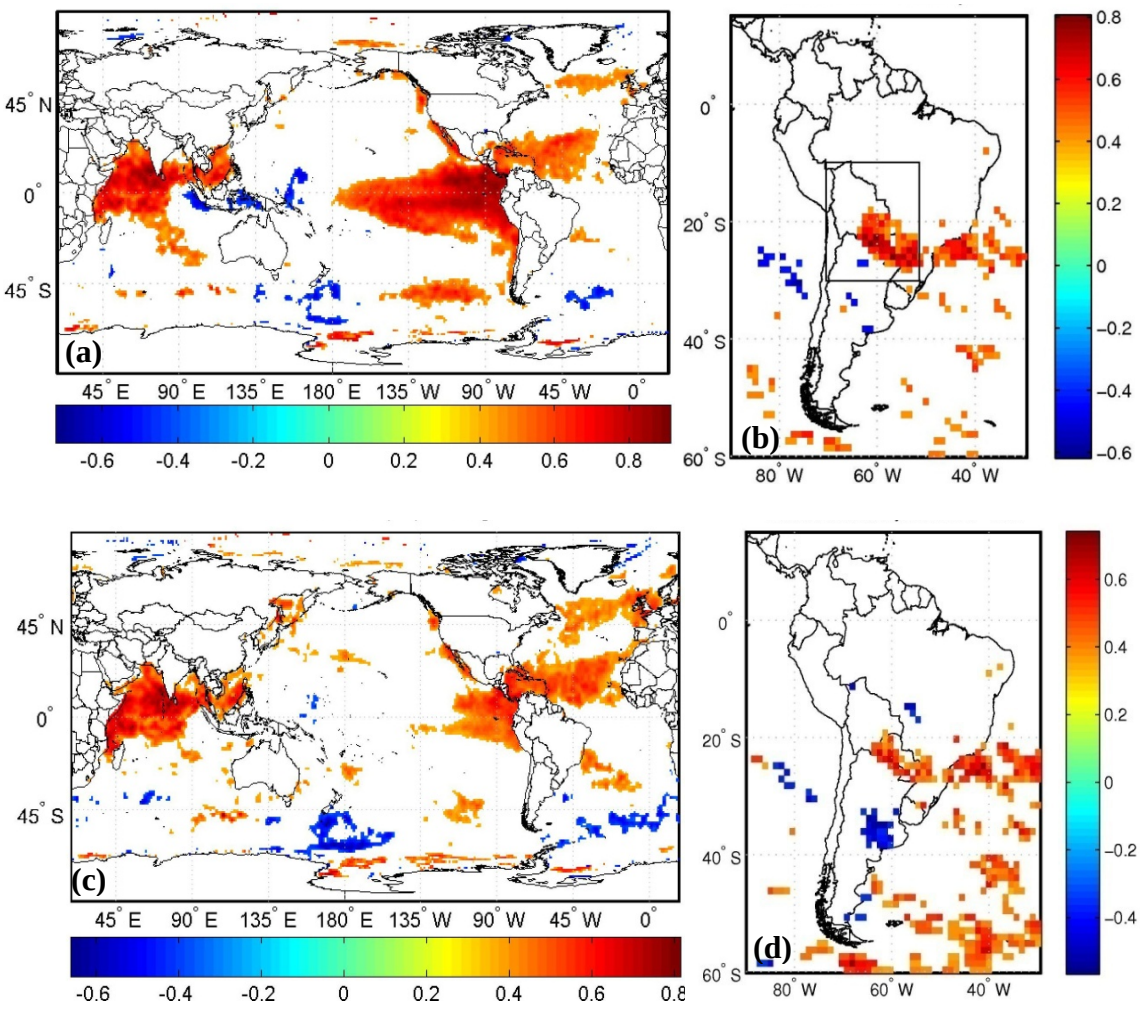

Figure 4.4. SON SVD2 homogeneous correlation maps spatial of (a) global SST anomalies and (b) CAI days. SST anomalies (c) and CAI (d) heterogeneous correlation maps. Shaded areas are 95% significant correlation in (a) and (b) and 90% significant correlation in (c) and (d).

The SST anomalies in the Indian Ocean stand out as a unique feature in this mode. The correlation between the two fields EC shows correlation of 0.79, the highest among the 3 modes presented (Figure 4.5).

In the Indian Ocean a strong zonal SST gradient between the tropical western and eastern basin defines the Indian Ocean Dipole (IOD) [*Saji et al.*, 1999; *Webster et al.*, 1999]. The strength of the zonal SST gradient anomaly is also referred to as the Dipole Mode Index (DMI). The DMI is calculated as the SST anomaly difference between the western (60^oE-80^oE,10^oS-10^oN) and eastern (90^oE-110^oE, 10^oS-0^o) Indian Ocean [*Saji et al.*, 1999]. Figure 4.6 shows that SST-EC2 time series is 95% significantly correlated to DMI (R=0.65).

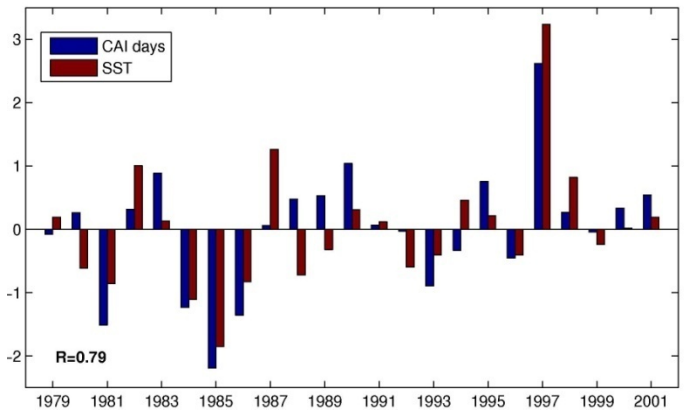

Figure 4.5. SST-EC2 and CAI-EC2 time series for the second mode of co-variability. The expansion coefficients are normalized by their respective standard deviations and are dimensionless.

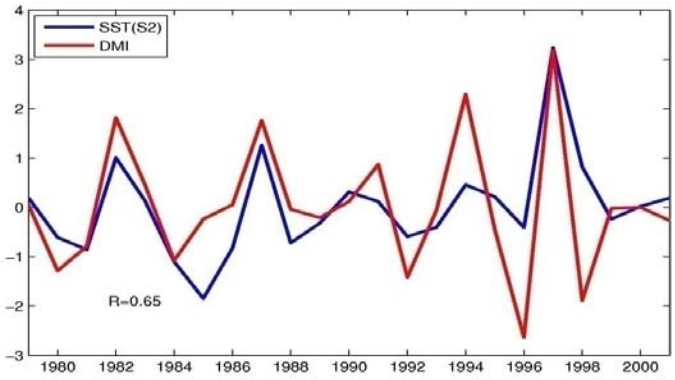

Figure 4.6. Dipole Mode Index (DMI) and SST-EC2 timeseries. The expansion coefficient is normalized by its standard deviations and is dimensionless.

The patterns of 250hPa zonal wind, storm track activity and geopotential associated with SVD2, as represented by the composite difference of these two fields associated with $\pm 1\sigma$ of the SST-EC2, reveal some interesting atmospheric features. The anomalous 250hPa geopotential height (Figure 4.7c) show a noteworthy area of positive height anomalies over Antarctica during the positive SVD2 phase (opposite sign for the negative SVD2 phase) which relates to a weak subpolar jet stream (Figure 4.7a). The subtropical jet stream on the other hand is stronger during the positive phase of SVD2 and crosses the South American continent around the latitude of 30^{o}S, defining only one clear transient wave guide. The absence of the high latitude wave guide along the subpolar jet stream favors an eventual merging of transients between the high and mid latitudes upon reaching the southern tip of South America, feature common to the effective displacement of transients onto subtropical and tropical latitudes [*Muller and Ambrizzi*, 2007; *Pezza and Ambrizzi*, 2005; *Vera and Vigliarolo*, 2000]. In fact the storm activity band (Figure 4.7b) turns northeastward upon reaching the southern tip of South America (yellow shades over Argentina), describing a pattern that is consistent with higher (lower) occurrence of CAI days during the positive (negative) phase of SVD2. The

greater occurrence of CAI days in this mode, however, concentrates to the south of 20^{o}S, having little impact in southern Amazon.

Despite the similarities of eastern tropical Pacific SST anomalies in this second mode of variability to those captured in SVD1 (see Figure 4.4a and Figure 4.1a), the area of SST anomalies upstream South America most relevant to CAI days variability seem to be located in the southern Indian Ocean (Figure 4.4c). This is consistent with previous studies showing that different stationary wave trains in the South Pacific respond to whether the main heat source is in the western tropical Pacific and/or in the Indian Ocean (see Figure 4.7c and Figure 4.3c) [*Drumond and Ambrizzi*, 2008; *Mo and Paegle*, 2001]. It should be noted that this mode seems to be driven by an extreme coupled pattern occurred in 1997, thus the warm and cold composites used in the differences consist of only three and two episodes respectively. The CAI days reconstructed from SVD2 does not show any significant trend for the period 1979-2001 in the Southern Amazon.

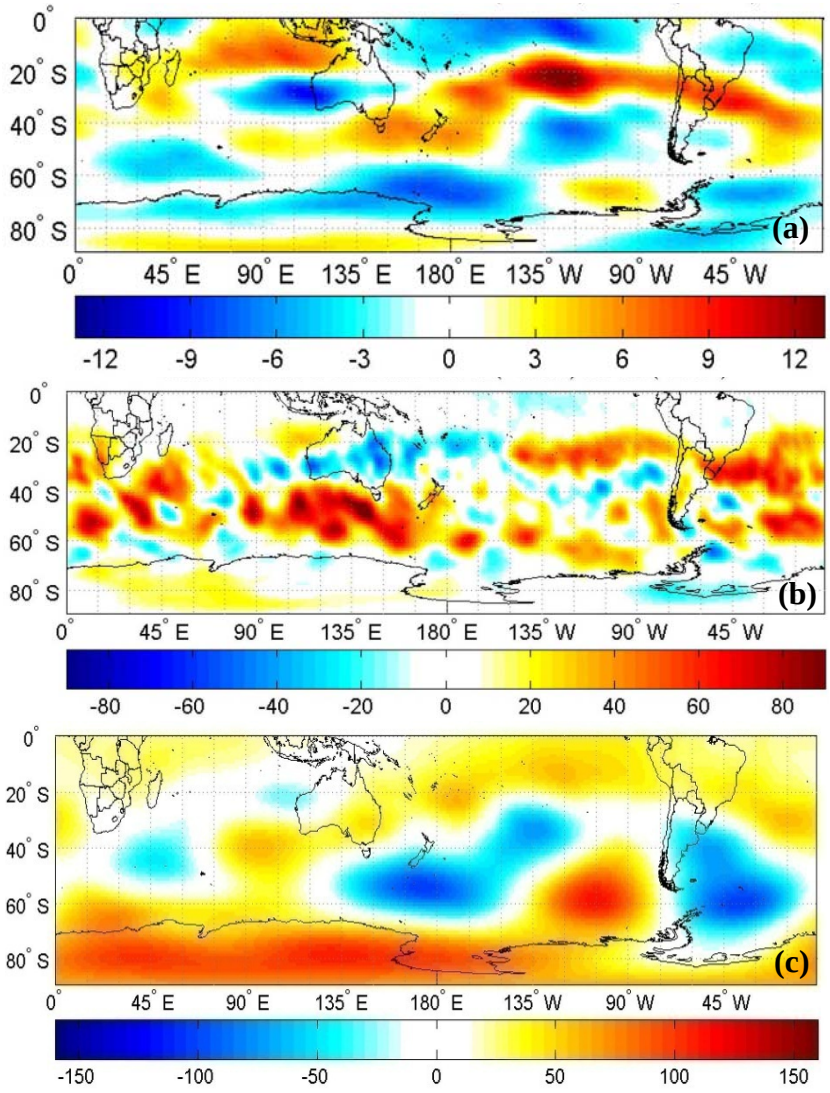

Figure 4.7. SON difference between composites in which SST-EC2 is above and below one standard deviation for 250 hPa (a) Zonal wind (U), (b) Storm track activity (v'^2) and (c) Geopotential height (Z). Units: U (m/s), v'^2(m^2/s^2) and Z (m).

4.3.3 Third Mode of Co-variability between SST and CAI days (SVD3)

The third mode of co-variability between SST anomalies and CAI days accounts for 17% of the total square covariance between SST anomalies and CAI days and 17% of total variance of CAI days in the domain 30^{o}S-10^{o}S and 70^{o}W-50^{o}W. The correlation between CAI days and SST expansion coefficients is 0.71, significant at the 95% level, revealing a strong coupling between SST and CAI variability.

The homogeneous correlation maps show lower occurrence of CAI days in central South America and negative (positive) SST anomalies in the eastern tropical (northern-extratropical) Pacific (Figure 4.8a and 4.8b). The heterogeneous correlation maps (Figure 4.8c) reveal that the most relevant SST anomalies are scattered, except for a large area in the northern Pacific and a dipole-like anomalies in the southern Indian Ocean. The northern Pacific area matches the area where the Pacific Decadal Oscillation signal is strongest and the dipole like mode resembles that of IOD. To further explore possible relationships between SST-EC3 and these phenomena a correlation to PDO index and DMI is conducted, which shows no significant correlation between SST-EC3 and DMI (0.29) but 95% significant correlation with PDO (-0.79) shown in Figure 4.9b. The PDO index is defined as the standardized leading principal component (PC) of the North Pacific monthly SST anomalies poleward of 20^{o}N for the 1900-93 period [*Mantua et al.*, 1997].

Evidence of South America climate regimes shifts and variability related to low frequency variability in the northern Pacific have been reported in literature, although mechanisms driving the observed responses in South America are not clear [*Agosta and*

Compagnucci, 2008; *Andreoli and Kayano*, 2005; *Chen et al.*, 2001; *Kayano and Andreoli*, 2007; *Marengo*, 2004; *Mestas-Nunez and Miller*, 2006].

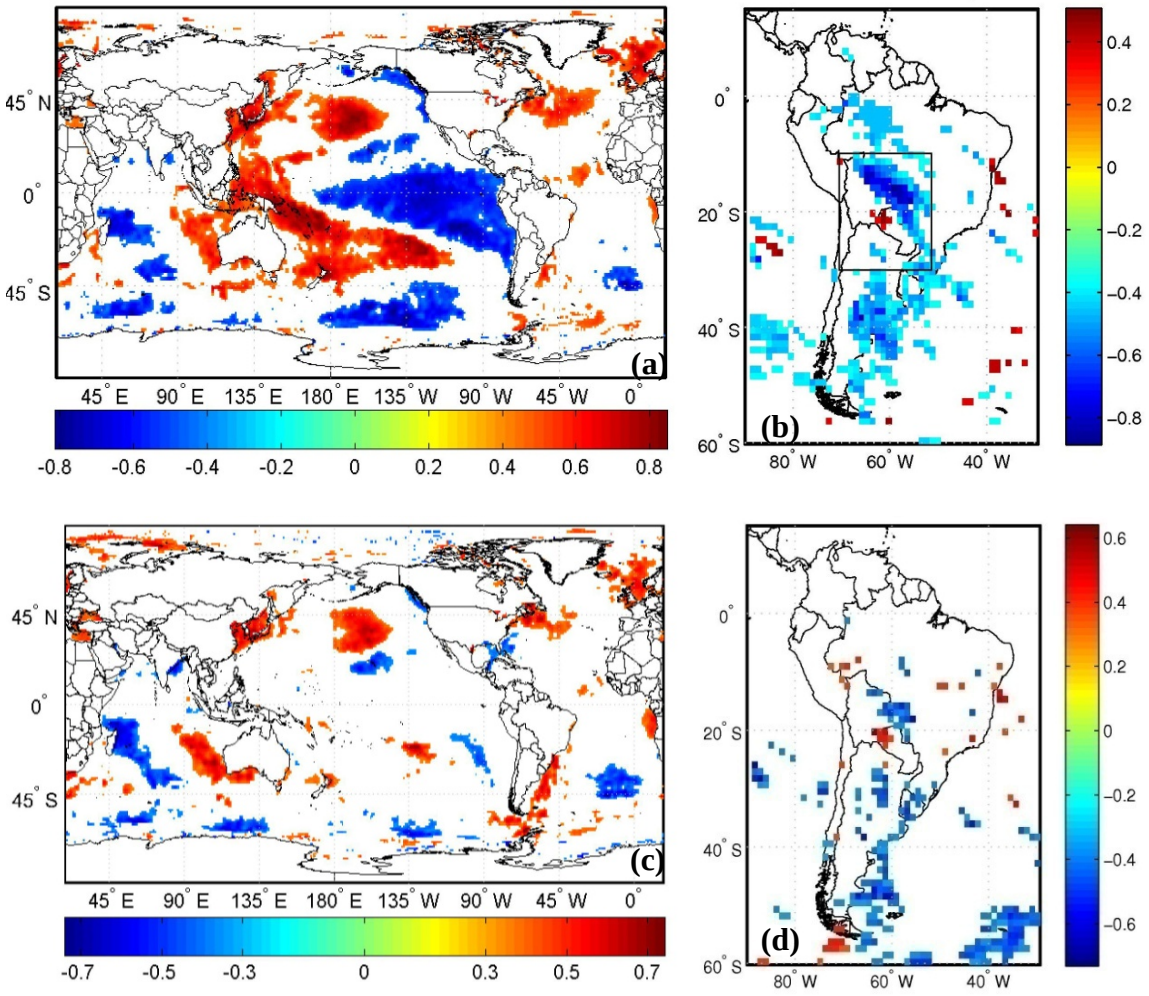

Figure 4.8. SON SVD3 homogeneous correlation maps spatial of (a) global SST anomalies and (b) CAI days. SST anomalies (c) and CAI (d) heterogeneous correlation maps. Shaded areas are 95% significant correlation in (a) and (b) and 90% significant correlation in (c) and (d).

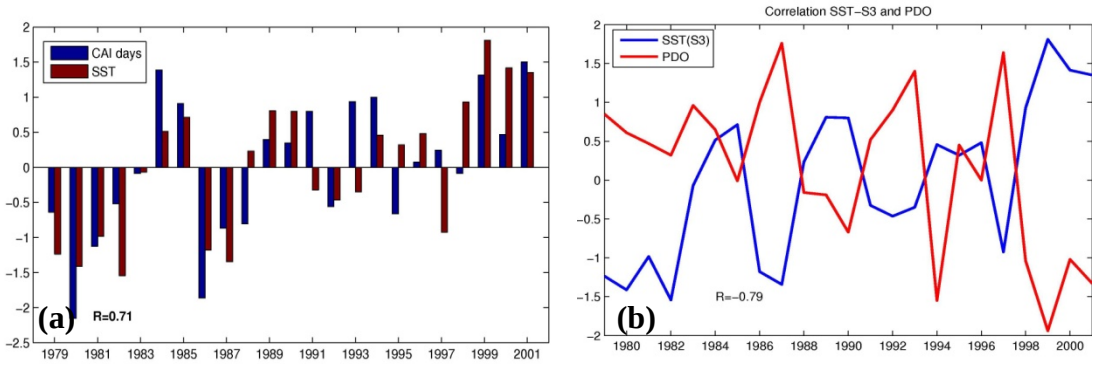

Figure 4.9. SST-EC3 and CAI-EC3 time series for the third mode of co-variability (a). Pacific Decadal Oscillation (PDO) index and SST-EC3 timeseries (b). Both SST-EC3 and PDO index are normalized by respective standard deviations and are dimensionless.

Even though the heterogeneous correlation map stresses the strongest PDO signal in the northern Pacific, which is expected by definition [*Mantua et al.*, 1997], the typical PDO also shows SST anomalies in the tropical Pacific in manner similar to that of ENSO. However, by evaluating the most general depiction of the co-variability between SST and CAI days in SVD1 (Figure 4.1a and b) and SVD3 (Figure 4.8a and b), a similar behavior in CAI days in southern Amazon is observed (lower occurrence of CAI days) related to the opposite SST behavior. Why a seemingly similar SST anomalies pattern between SVD1 and SVD3 appear to have opposite influence on CAI in South America? In order to isolate the differences in behavior observed in CAI days related to each mode's SST anomalies, a comparison side by side of some atmospheric variables and SST anomalies is presented. The SVD3 results shown in Figure 4.10 represent the difference of composites with respect to the years below -1σ and above $+1\sigma$ of SST-EC3 timeseries. Note that SST-EC3 is anticorrelated with PDO, so the $-1\sigma\,(+1\sigma)$ SST-EC3 relates to positive (negative PDO) or warm (cold) eastern tropical Pacific SST. For simplicity both

SVD1 and SVD3 composites difference will be referred to as warm-cold referring to eastern Pacific SST anomalies.

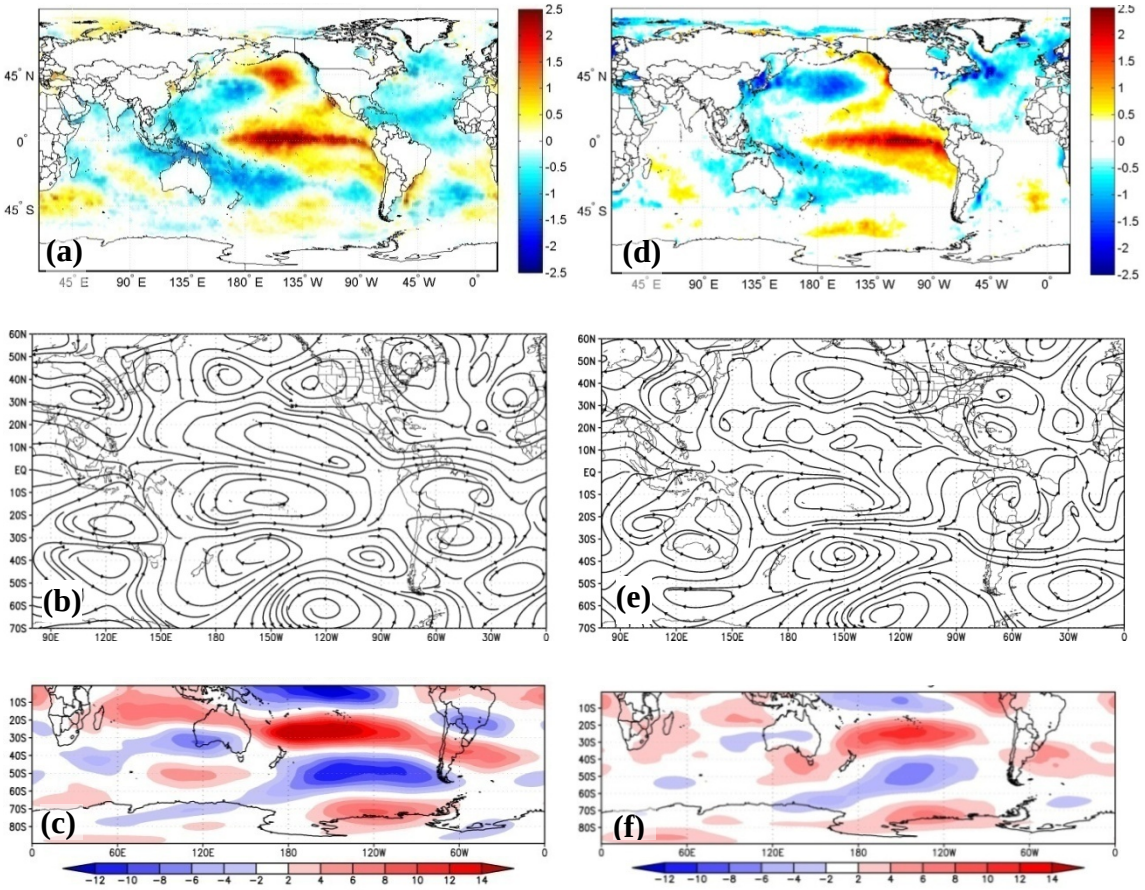

Figure 4.10. SON difference between SVD1 warm and cold phases of (a) Sea Surface Temperature (^{o}C), (b) 250hPa streamlines (m/s) (c) 250hPa zonal wind component (m/s). (d) Same as (a), (e) same as (b) and (f) same as (c) for SVD3.

The warm-cold composites of SVD1 SST show a typical El Niño pattern (or La Niña with sign reversed) pattern of SST anomalies (Figure 4.10a), with warm water waters extending from the central Pacific to the western coast of South America. In contrast, the anomalous warmer waters associated with SVD3 (sign reversed for cold SVD3) are concentrated to the east of 135^{o}W (Figure 4.10d).

In the upper troposphere, the 250hPa streamlines shows an anomalous anticyclone in the SVD1 warm-cold composites over southern Brazil and Uruguay (Figure 4.10b), consistent with rainier seasons in that region during El Niño [*Grimm et al.*, 1998]. An upper level cyclone in northeastern Brazil is as well characteristic of ENSO warm phase, result of the eastward displaced Walker Cell and subsidence branch over the region [*Kousky et al.*, 1984; *Ropelewski and Halpert*, 1987]. The SVD3 warm-cold composite however, shows an anomalous cyclonic circulation or a weaker Bolivian High over central Brazil, accompanied by upper level divergence in northeastern Brazil (Figure 4.10e). The 250hPa anomalous zonal wind patterns, despite some resemblance over the Pacific and Indian Oceans, show that the strong subtropical jet stream crossing South America seen in SVD3 (Figure 4.10e) is not nearly as strong as that of SVD1 (Figure 4.10c), which is consistent with milder SST anomalies in the tropical Pacific associated with the third mode (Figure 4.10 d).

The atmospheric link between the tropical Pacific and South America may occur in the form of southeastwardly propagating waves originated in the western Pacific in response to anomalous convection. These waves then curve toward the northeast over South America and are referred to as the Pacific South American (PSA) modes. PSA1 and PSA2 modes appear in all seasons showing slight variation in the loading centers

location in the tropical Pacific [*Karoly*, 1989; *Kidson*, 1999; *Mo and Paegle*, 2001; *NoguesPaegle and Mo*, 1997]. A PSA1 like wave train is seen in the SVD1 250hPa streamfunction composite differences, shown in Figure 4.11a. It is triggered initially by anomalous convection in the central-western Pacific due to El Niño, and then extends southeastward toward Antarctica curving northeastward upon reaching South America. In South America it defines an 250hPa anticyclone (cyclone) over southern Brazil during El Niño (La Niña) years. The strong subtropical jet stream observed in southern South America during El Niño years is co-located with the southern edge of this anticyclone (Figure 4.10c). During La Niña years the anomalies are the opposite of El Niño. This feature is in agreement with the reduced (increased) CAI days during El Niño (La Niña) years, revealing a stronger (weaker) subtropical jet stream that blocks (offers no resistant) to northward displacement of transients.

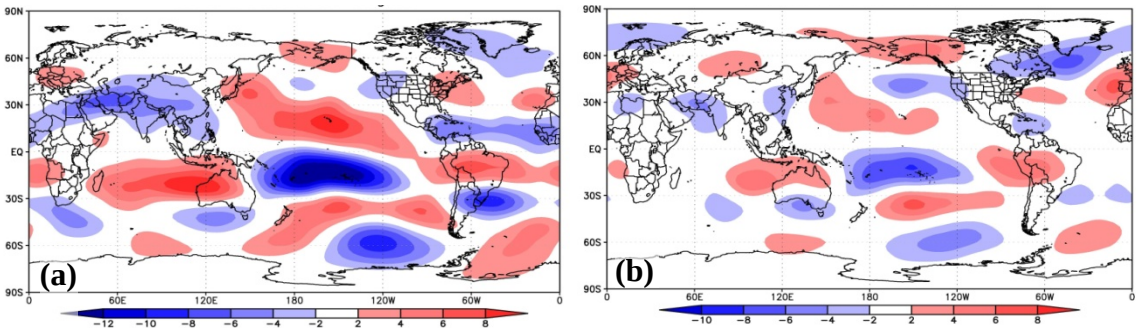

Figure 4.11. SON difference between warm and cold phases of 250hPa eddy streamfunction with zonal means removed for (a) SVD1 and (b) SVD3. Filled contour interval is 2 x 10^6 m^2/s.

The SVD3 streamfunction composites difference on the other hand, also shows a wave train from central-western Pacific toward Antarctica, but it does not curve back

northeastward to South America, revealing a much more zonally symmetric feature. This pattern resembles that found by *Garreaud and Battisti* [1999] showing that the 500hPa geopotential height regressed upon their purely decadal ENSO-like mode has a much more zonally symmetric characteristic than that of ENSO in the southern Pacific.

The anomalous anticyclone (cyclone) in southern Brazil during the El Niño (La Niña) is inexistent during positive (negative) PDO phases and consistent with the milder anomalies observed in the subtropical jet stream over southern Brazil and Argentina in the SVD3 difference composites (Figure 4.10f). On the other hand, the cyclonic circulation observed over tropical South America (pink shades) is observed in SVD1 and SVD3 difference composites, indicating upper level convergence or a weakening effect on the Bolivian High.

The similar cyclonic pattern observed over tropical South America seems to have the same root in the Pacific by ways of an anomalous Walker Cell. The velocity potential, which is a scalar function with its gradient equal to the divergent component of the wind, is useful to identify areas of large scale convergence and divergence, thus used here to identify Walker Cell variations (Figure 4.12). Although an overall area of upper atmosphere convergence over tropical South America (positive velocity potential values in Figure 4.12a and b) is common to both SVD1 and SVD3 composites, the precise area of stronger subsidence differs substantially between the 2 modes. The SVD1 composites difference (Figure 4.12a) shows a large area of 250hPa divergence (or convection) in the central Pacific, related to the broad area of SST anomalies during the warm phase of ENSO. The flow in central Pacific then converges in Indonesia and northern South America. In the SVD3 case, a 250hPa divergent flow is also seen as a result of the

warmer SST anomalies, although the divergent area is reduced and spread southward. This slightly southwestward position of the 250hPa divergent flow seems to cause the downward branch of the Walker Cell in tropical South America (pink shades in Figure 4.12b) to be also located slightly southwestward when compared to the SVD1 composite. Consequently, a weakened Bolivian High during positive PDO events is favored, defining an upper atmosphere condition favorable to CAI in central South America. This is consistent with the findings of Lenters and Cook [1999], showing that a weakened Bolivian High favors the incursion of cold air over the Bolivian Plateau as well enhanced convection over southern Amazon.

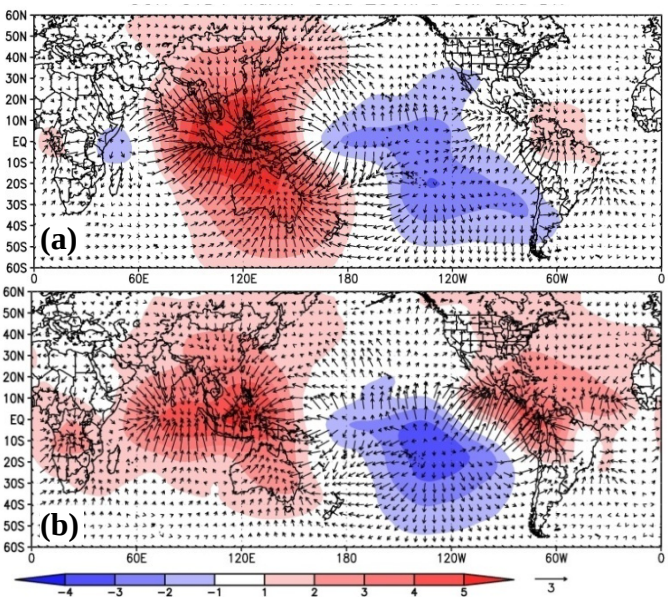

Figure 4.12. SON difference between warm and cold phases 250hPa velocity potential (shaded) and divergent component of the wind (vectors) for (a) SVD1 and (b) SVD3. Shaded contour intervals are $1x10^6$ m^2/s. Three m/s vectors are scaled at the bottom.

Finally, the CAI days reconstructed from SVD3 shows a 95% significant trend of as much as 1.5 one day per season per decade in southern Amazon (Figure 4.13), in

general agreement with the spatial distribution of CAI days negative trend shown in Figure 3.9a. An upper atmosphere pattern consistent with that of positive SVD3, would result in near normal subtropical jet stream crossing South America as well as a weaker Bolivian High, effects that describe a favorable pattern for CAI incursion into central South America. The opposite sign SVD3 atmospheric pattern on the other hand, would affect CAI in the opposite way. The observed 95% positive SST-EC3 positive trend (coinciding with a 95% negative trend in PDO index) is in agreement with the SVD3 reconstructed CAI days.

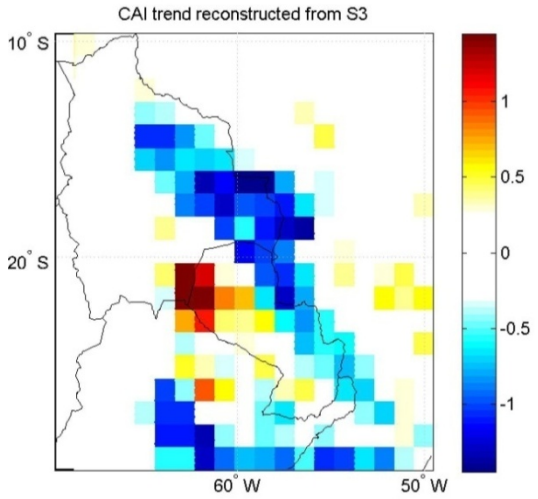

Figure 4.13 Trends in CAI days reconstructed from the third SVD mode. Shaded grids are 95% significant trends. Unit: Days per season per decade.

4.4 Discussion and Conclusions

Three modes of co-variability were identified between CAI days and global SST. The first mode of co-variability describes the relationship of El Niño (La Niña) with lower (greater) occurrence of CAI days in southern Amazon. A sharper (weaker)

meridional temperature gradient over the southern Pacific in El Niño (La Niña) years result in a stronger (weaker) Subtropical Jet Stream crossing South America working unfavorably (favorably) to the displacement of transient waves into subtropical latitudes.

The second mode of co-variability, describes a mode in which greater occurrence of CAI days is observed to the south of 20^{o}S in central South America in conjunction with warmer tropical Pacific and Indian Oceans. Transient systems propagating along the subtropical jet stream and over high latitudes in the southern Pacific, tend to merge upon reaching the southern tip of South America then move northward into the central part of the continent. Neither CAI days reconstructed from the SVD1 nor SVD2 modes present a significant trend in CAI days in southern Amazon.

The third SVD mode depicts the SST anomaly pattern resembling PDO, showing anomalous SST in the tropical eastern Pacific accompanied by anomalous SST of opposite sign in the northern extratropical Pacific. The similarities of SST distribution during same phase ENSO and PDO would at a first glance suggest similar responses in the South American climate. However, during warm eastern Pacific SST in SVD1 and SVD3 the number of days per season under cold air influence presents the opposite behavior. The atmospheric patterns seem to indicate that:

i) During the warm phase of ENSO, a wave train originating in the western tropical Pacific moves toward South America, resulting in an anomalous upper atmophere anticyclonic circulation that contributes to the enhancement of the subtropical jet stream over southern Brazil and Argentina. This feature is non-existent during the warm phase of SVD3 (warm SST in eastern Pacific) since South America is not in the path of the wave train that originates in the Pacific, thus the intensification of the subtropical jet stream

does not occur by means of Rossby wave propagation. Extratropical transient systems encounter less of an obstacle (near normal-jet) to its northward displacement.

ii) The effect of a southwestward shifted upward branch of the Walker Cell, results in an also shifted to the west descending branch over South America, in the area of the Bolivian High. A weaker Bolivian high favors the northward displacement of CAI into southern Amazon.

A negative trend in the PDO timeseries towards the end of the 1990s, is in agreement with a decreasing trend in the CAI days in South America. In fact, CAI days reconstructed from this SVD3 shows a 95% significant trend of 1 day and higher per decade in CAI days in southern Amazon. Therefore, studies of climate variability and change in South America should consider the implications of PDO phase change, which in the case of austral spring CAI seem to work in opposite direction of that of ENSO especially in subtropical latitudes. It should be stressed however that the 23 years used in this study does not constitute a timeseries long enough for us to conclusively attribute the SVD3 behavior to PDO.

CHAPTER 5

CONCLUSIONS AND FUTURE DIRECTIONS

In this Dissertation we determined how well the Amazon water budget can be estimated based on observational and reanalysis data. The results suggest that annual precipitation integrated over the Amazon is well estimated in ERA40 although this is result of precipitation underestimation during the wet season and overestimation during the dry season when compared to CPC data. Annual runoff in the reanalysis underestimates the streamflow near the Amazon's mouth by an average of 25%, presumably due to an excessive canopy interception, which would result in excessive ET and reduced soil moisture storage. Evidence that ET may be overestimated in the reanalysis is seen when individual tower measurements are compared to point ERA40 ET, indicating a 20% positive bias, higher than ET measurements uncertainty (~10%). To maintain a realistic ET, soil moisture is added to the land surface upper layer (one meter deep) during the dry season. However, the Amazon forest drawdown can go to depths of 3 meters, suggesting the ERA40 land surface model may not be suited to represent the Amazon vegetation. A simple scaling of ERA40 ET to tower measurements, results in a more realistic estimate when compared to that from the residual between basin wide precipitation and streamflow. In synthesis, my findings suggest that surface water budget variables estimates can be reliably obtained from observations and ERA40 on annual timescales. Caution should be exercised when evaluating the basin averaged seasonal cycle and spatial distribution of precipitation.

Changes in the hydrological cycle and weather patterns in the Amazon during the past few decades were investigated by evaluating the variability of the wet season onset timing and incursion of cold air into southern Amazon. A seasonal CAI index relates inversely to the time of the onset, indicating that lower occurrence of CAI in southern Amazon correlates with later onset. An evaluation of anomalously early and late onset episodes reveals that early onsets are often preceded by a regular income of CAI events during September and early October. This process, along with a more favorable thermodynamic condition in the lower troposphere produces large-scale rainfall, which further destabilizes the troposphere, increasing soil moisture leading to a rapid circulation transition to wet season. Finally, the passage of another cold front suddenly triggers convection and precipitation to above the threshold values for the onset definition. During the late onset, CAI events are sparser and not as intense as those observed during the early onset, with the added characteristic of almost no occurrence of CAI events during October. A decreasing number of CAI days in southern Amazon is observed in September for the same period of the wet season onset delaying trend, consistent with the assumption that lower number of CAI early in the season will result in a delayed occurrence of sustained convection.

The large scale mechanism controlling the variability and trend of CAI days in southern Amazon is found to be related to tropical forcings upstream of South America. CAI days in southern Amazon during SON is strongly coupled to the El Niño Southern Oscillation (ENSO), mode of co-variability explaining 34% of the total covariance between CAI days and SST anomalies. A stronger subtropical jet stream acts to block or deflect transient waves moving into South America, causing a reduction (increase) in

CAI day during El Niño (La Niña) years. The analysis of gridded CAI provides a broader picture of how ENSO affects both the frequency and spread of incoming cold air masses in South America. The first mode of co-variability is not related to the decreasing trend in CAI days in the region.

A shift in the position of the most relevant SST anomalies towards the Indian ocean and eastern Pacific, defines the spatial pattern of the SST second mode of variability. The resulting CAI days response is now concentrated to the south of 20^{o}S, indicating increased (decreased) CAI days during the positive (negative) phase of this mode. Stormtracks describe a preferential path for transient Rossby waves veering northwards to northern Argentina upon reaching the southern tip of South America consistent with the CAI behavior observed. CAI days reconstructed from this mode does not result in any significant trend in CAI days.

The third mode of co-variability describes SST anomalies in the northern and tropical Pacific associated with CAI days. Composites showing the difference between the extreme events of this mode reveal SST patterns similar to those observed during SVD1. The timeseries of this mode present high correlation with the Pacific Decadal Oscillation Index, showing milder and shifted eastward SST anomalies in the equatorial Pacific, as compared to SVD1. The apparent similarities in the SVD1 and SVD3 SST composites result in a rather different Rossby wave train in the southern Pacific. A typical upper atmosphere anticyclone over southern Brazil during ENSO, which works to strengthen the subtropical jet stream (consequently blocking CAI) is absent during positive PDO, describing a more favorable environment for northward of CAI events. Additionally, the anomalous Walker cell describing an upper atmosphere cyclonic

circulation over NE Brazil during El Niño, now is shifted to the west over the Bolivian High area working to weaken the upper troposphere anticyclone. A weaker Bolivian High is consistent with northward displacement of cold air and the opposite behavior would be observed during the cold phase of SVD3 (colder eastern Pacific). Therefore, the observed negative trend in PDO during 1979-2001 agrees with a decreasing trend in CAI days in southern Amazon consistent as well with a delaying wet season onset. It should be stressed that the relatively short time series used in this study prevents us from conclusively attribute the third mode of variability to PDO, although the spatial SST pattern and PDO index timeseries are consistent with those obtained in our analysis.

The Amazon climate is complex and predicting the quality of the wet season is a challenge. In a scenario of Global Climate Change, understanding the various large scale forcing to the Amazon regional climate can potentially improve model interpretation and extend predictability. *Li and Fu* [2006], have found that the Amazon precipitation and seasonality are predicted quite differently among the Intergovernmental Panel for Climate Change fourth assessment report (IPCC-AR4) models. Could the different changes in seasonality amongst models be related to large-scale variability in CAI in future climate? Some studies have shown that extratropical storm tracks are predicted to shift poleward [*Bengtsson et al.*, 2006], whereas the increase in CO2 concentration would lead to increase in strong cyclones density in the Southern Hemisphere [*Geng and Sugi*, 2003]. To investigate whether CAI days in central South America are predicted to change in future climate, I propose to evaluate how the IPCC-AR4 (and possibly IPCC-AR5 expected to be released to the community in January 2010), models compare to the CAI days statistics found in this work so to isolate the models that better represent current

conditions. I also propose to verify whether the current large-scale forcings that determine the changes of the CAI in southern Amazon are adequately simulated in the models. The seasonality of the Amazon precipitation can then be verified against the potential change of weather patterns in the southern Amazon to assess the impact of midlatitude climate change on the tropical South America in future climate scenarios.

REFERENCES

Adler, R. F., G. J. Huffman, D. T. Bolvin, S. Curtis, and E. J. Nelkin (2000), Tropical rainfall distributions determined using TRMM combined with other satellite and rain gauge information, *Journal of Applied Meteorology*, *39*(12), 2007-2023.

Adler, R. F., G. J. Huffman, A. Chang, R. Ferraro, P. P. Xie, J. Janowiak, B. Rudolf, U. Schneider, S. Curtis, D. Bolvin, A. Gruber, J. Susskind, P. Arkin, and E. Nelkin (2003), The version-2 global precipitation climatology project (GPCP) monthly precipitation analysis (1979-present), *Journal of Hydrometeorology*, *4*(6), 1147-1167.

Agosta, E. A., and R. H. Compagnucci (2008), The 1976/77 austral summer climate transition effects on the atmospheric circulation and climate in southern South America, *Journal of Climate*, *21*(17), 4365-4383.

Ambrizzi, T., B. J. Hoskins, and H. H. Hsu (1995), Rossby-Wave Propagation and Teleconnection Patterns in the Austral Winter, *Journal of the Atmospheric Sciences*, *52*(21), 3661-3672.

Anagnostou, E. N., and C. A. Morales (2002), Rainfall estimation from TOGA radar observations during LBA field campaign, *Journal of Geophysical Research-Atmospheres, 107*(D20), DOI: 10.1029/2001JD000377.

Andreoli, R. V., and M. T. Kayano (2005), Enso-related rainfall anomalies in South America and associated circulation features during warm and cold Pacific Decadal Oscillation regimes, *International Journal of Climatology*, *25*(15), 2017-2030.

Bengtsson, L., K. I. Hodges, and E. Roeckner (2006), Storm tracks and climate change, *Journal of Climate*, *19*(15), 3518-3543.

Berbery, E. H., and C. S. Vera (1996), Characteristics of the Southern Hemisphere winter storm track with filtered and unfiltered data, *Journal of the Atmospheric Sciences*, *53*(3), 468-481.

Betts, A. K., J. H. Ball, and P. Viterbo (2003), Evaluation of the ERA-40 surface water budget and surface temperature for the Mackenzie River basin, *Journal of Hydrometeorology*, *4*(6), 1194-1211.

Betts, A. K., J. H. Ball, P. Viterbo, A. G. Dai, and J. Marengo (2005), Hydrometeorology of the Amazon in ERA-40, *Journal of Hydrometeorology*, *6*(5), 764-774.

Betts, A. K., J. H. Ball, A. G. Barr, T. A. Black, J. H. McCaughey, and P. Viterbo (2006), Assessing land-surface-atmosphere coupling in the ERA-40 reanalysis with boreal forest data, *Agricultural and Forest Meteorology*, *140*(1-4), 365-382.

Bevan, S. L., P. R. J. North, W. M. F. Grey, S. O. Los, and S. E. Plummer (2009), Impact of atmospheric aerosol from biomass burning on Amazon dry-season drought, *Journal of Geophysical Research-Atmospheres*, *114*.

Bjornsson, H., and S. A. Venegas (1997), A manual for EOF and SVD analyses of climate data, 52 pp, McGill University, Montreal.

Bretherton, C. S., C. Smith, and J. M. Wallace (1992), An intercomparison of methods for finding coupled patterns in climate data, *Journal of Climate*, *5*(6), 541-560.

Cavalcanti, I. F. A., and V. E. Kousky (2003), Climatology of South American Cold Fronts, paper presented at VII International Conference on Southern Hemisphere Meteorology and Oceanography, AMS, Wellington, New Zealand.

Chan, S. C., S. K. Behera, and T. Yamagata (2008), Indian Ocean Dipole influence on South American rainfall, *Geophysical Research Letters*, *35*(14).

Chang, E. K. M. (2004), Are the Northern Hemisphere winter storm tracks significantly correlated?, *Journal of Climate*, *17*(21), 4230-4244.

Chapelon, N., H. Douville, P. Kosuth, and T. Oki (2002), Off-line simulation of the Amazon water balance: a sensitivity study with implications for GSWP, *Climate Dynamics*, *19*(2), 141-154.

Chen, M. Y., P. P. Xie, J. E. Janowiak, and P. A. Arkin (2002), Global land precipitation: A 50-yr monthly analysis based on gauge observations, *Journal of Hydrometeorology*, *3*(3), 249-266.

Chen, T. C., J. H. Yoon, K. J. St Croix, and E. S. Takle (2001), Suppressing impacts of the Amazonian deforestation by the global circulation change, *Bulletin of the American Meteorological Society*, *82*(10), 2209-2216.

Coe, M. T. (2000), Modeling terrestrial hydrological systems at the continental scale: Testing the accuracy of an atmospheric GCM, *Journal of Climate*, *13*(4), 686-704.

Comeaux, J. L., and S. J. Worley (2005), ECMWF 45-Year Reanalysis Data from NCAR, paper presented at The 85th AMS Annual Meeting, AMS, San Diego, CA.

Costa, M. H., and J. A. Foley (1998), A comparison of precipitation datasets for the Amazon basin, *Geophysical Research Letters*, *25*(2), 155-158.

Cox, P. M., R. A. Betts, M. Collins, P. P. Harris, C. Huntingford, and C. D. Jones (2004), Amazonian forest dieback under climate-carbon cycle projections for the 21st century, *Theoretical and Applied Climatology*, *78*(1-3), 137-156.

Cox, P. M., P. P. Harris, C. Huntingford, R. A. Betts, M. Collins, C. D. Jones, T. E. Jupp, J. A. Marengo, and C. A. Nobre (2008), Increasing risk of Amazonian drought due to decreasing aerosol pollution, *Nature*, *453*(7192), 212-U217.

CPC (2009), Cold and warm ENSO episodes by season, edited by NOAA, http://www.cpc.noaa.gov/products/analysis_monitoring/ensostuff/ensoyears.shtml

Cutrim, E. M. C., D. W. Martin, D. G. Butzow, I. M. Silva, and E. Yulaeva (2000), Pilot analysis of hourly rainfall in central and eastern Amazonia, *Journal of Climate*, *13*(7), 1326-1334.

Dai, A. G., and K. E. Trenberth (2002), Estimates of freshwater discharge from continents: Latitudinal and seasonal variations, *Journal of Hydrometeorology*, *3*(6), 660-687.

Diaz, A. F., C. D. Studzinski, and C. R. Mechoso (1998), Relationships between precipitation anomalies in Uruguay and southern Brazil and sea surface temperature in the Pacific and Atlantic oceans, *Journal of Climate*, *11*(2), 251-271.

Douville, H., P. Viterbo, J. F. Mahfouf, and A. C. M. Beljaars (2000), Evaluation of the optimum interpolation and nudging techniques for soil moisture analysis using FIFE data, *Monthly Weather Review*, *128*(6), 1733-1756.

Drumond, A., and T. Ambrizzi (2008), The role of the South Indian and Pacific oceans in South American monsoon variability, *Theoretical and Applied Climatology*, *94*(3-4), 125-137.

Eltahir, E. A. B., and R. L. Bras (1994), Precipitation Recycling in the Amazon Basin, *Quarterly Journal of the Royal Meteorological Society*, *120*(518), 861-880.

Fernandes, K., R. Fu, and A. K. Betts (2008), How well does the ERA40 surface water budget compare to observations in the Amazon River basin?, *Journal of Geophysical Research-Atmospheres*, *113*(D11).

Field, C. B., M. J. Behrenfeld, J. T. Randerson, and P. Falkowski (1998), Primary production of the biosphere: Integrating terrestrial and oceanic components, *Science*, *281*(5374), 237-240.

Finnigan, J. J., R. Clement, Y. Malhi, R. Leuning, and H. A. Cleugh (2003), A re-evaluation of long-term flux measurement techniques - Part I: Averaging and coordinate rotation, *Boundary-Layer Meteorology*, *107*(1), 1-48.

Foken, T., F. Wimmer, M. Mauder, C. Thomas, and C. Liebethal (2006), Some aspects of the energy balance closure problem, *Atmospheric Chemistry and Physics*, *6*, 4395-4402.

Fu, R., B. Zhu, and R. E. Dickinson (1999), How do atmosphere and land surface influence seasonal changes of convection in the tropical amazon?, *Journal of Climate*, *12*(5), 1306-1321.

Fu, R., R. E. Dickinson, M. X. Chen, and H. Wang (2001), How do tropical sea surface temperatures influence the seasonal distribution of precipitation in the equatorial Amazon?, *Journal of Climate*, *14*(20), 4003-4026.

Fu, R., and W. Li (2004), The influence of the land surface on the transition from dry to wet season in Amazonia, *Theoretical and Applied Climatology*, *78*(1-3), 97-110.

Fung, I. Y., S. C. Doney, K. Lindsay, and J. John (2005), Evolution of carbon sinks in a changing climate, *Proceedings of the National Academy of Sciences of the United States of America*, *102*(32), 11201-11206.

Garreaud, R. D. (1999), Cold air incursions over subtropical and tropical South America: A numerical case study, *Monthly Weather Review*, *127*(12), 2823-2853.

Garreaud, R. D., and D. S. Battisti (1999), Interannual (ENSO) and interdecadal (ENSO-like) variability in the Southern Hemisphere tropospheric circulation, *Journal of Climate*, *12*(7), 2113-2123.

Garreaud, R. D. (2000), Cold air incursions over subtropical South America: Mean structure and dynamics, *Monthly Weather Review*, *128*(7), 2544-2559.

Geng, Q. Z., and M. Sugi (2003), Possible change of extratropical cyclone activity due to enhanced greenhouse gases and sulfate aerosols - Study with a high-resolution AGCM, *Journal of Climate*, *16*(13), 2262-2274.

Grimm, A. M., S. E. T. Ferraz, and J. Gomes (1998), Precipitation anomalies in southern Brazil associated with El Nino and La Nina events, *Journal of Climate*, *11*(11), 2863-2880.

Hagemann, S., and L. D. Gates (2003), Improving a subgrid runoff parameterization scheme for climate models by the use of high resolution data derived from satellite observations, *Climate Dynamics*, *21*(3-4), 349-359.

Hansen, J., M. Sato, R. Ruedy, K. Lo, D. W. Lea, and M. Medina-Elizade (2006), Global temperature change, *Proceedings of the National Academy of Sciences of the United States of America*, *103*(39), 14288-14293.

Hastenrath, S. (1990), Prediction of northeast Brazil rainfall anomalies, *Journal of Climate*, *3*(8), 893-904.

Haylock, M. R., T. C. Peterson, L. M. Alves, T. Ambrizzi, Y. M. T. Anunciacao, J. Baez, V. R. Barros, M. A. Berlato, M. Bidegain, G. Coronel, V. Corradi, V. J. Garcia, A. M. Grimm, D. Karoly, J. A. Marengo, M. B. Marino, D. F. Moncunill, D. Nechet, J. Quintana, E. Rebello, M. Rusticucci, J. L. Santos, I. Trebejo, and L. A. Vincent (2006), Trends in total and extreme South American rainfall in 1960-2000 and links with sea surface temperature, *Journal of Climate*, *19*(8), 1490-1512.

Huffman, G. J., R. F. Adler, D. T. Bolvin, G. J. Gu, E. J. Nelkin, K. P. Bowman, Y. Hong, E. F. Stocker, and D. B. Wolff (2007), The TRMM multisatellite

precipitation analysis (TMPA): Quasi-global, multiyear, combined-sensor precipitation estimates at fine scales, *Journal of Hydrometeorology*, *8*(1), 38-55.

Juarez, R. I. N., M. G. Hodnett, R. Fu, M. L. Goulden, and C. von Randow (2007), Control of dry season evapotranspiration over the Amazonian forest as inferred from observations at a southern Amazon forest site, *Journal of Climate*, *20*(12), 2827-2839.

Karoly, D. J. (1989), Southern-Hemisphere Circulation Features Associated with Elnino - Southern Oscillation Events, *Journal of Climate*, *2*(11), 1239-1252.

Kayano, M. T., and R. V. Andreoli (2007), Relations of South American summer rainfall interannual variations with the Pacific Decadal Oscillation, *International Journal of Climatology*, *27*(4), 531-540.

Kendall, M. G. (1938), A new measure of rank correlation, *Biometrika*, *30*, 81-93.

Kidson, J. W. (1999), Principal modes of Southern Hemisphere low-frequency variability obtained from NCEP-NCAR reanalyses, *Journal of Climate*, *12*(9), 2808-2830.

Kidson, J. W., M. J. Revell, B. Bhaskaran, A. B. Mullan, and J. A. Renwick (2002), Convection patterns in the tropical Pacific and their influence on the atmospheric circulation at higher latitudes, *Journal of Climate*, *15*(2), 137-159.

Kousky, V. E., M. T. Kagano, and I. F. A. Cavalcanti (1984), A review of the Southern Oscillation - Oceanic-Atmospheric circulation changes and related rainfall anomalies, *Tellus Series a-Dynamic Meteorology and Oceanography*, *36*(5), 490-504.

Kumar, K. K., B. Rajagopalan, M. Hoerling, G. Bates, and M. Cane (2006), Unraveling the mystery of Indian monsoon failure during El Nino, *Science*, *314*(5796), 115-119.

Kummerow, C., J. Simpson, O. Thiele, W. Barnes, A. T. C. Chang, E. Stocker, R. F. Adler, A. Hou, R. Kakar, F. Wentz, P. Ashcroft, T. Kozu, Y. Hong, K. Okamoto, T. Iguchi, H. Kuroiwa, E. Im, Z. Haddad, G. Huffman, B. Ferrier, W. S. Olson, E. Zipser, E. A. Smith, T. T. Wilheit, G. North, T. Krishnamurti, and K. Nakamura (2000), The status of the Tropical Rainfall Measuring Mission (TRMM) after two years in orbit, *Journal of Applied Meteorology*, *39*(12), 1965-1982.

LeFavour, G., and D. Alsdorf (2005), Water slope and discharge in the Amazon River estimated using the shuttle radar topography mission digital elevation model, *Geophysical Research Letters, 32*(17), DOI: 10.1029/2005GL023836.

Lenters, J. D., and K. H. Cook (1999), Summertime precipitation variability over South America: Role of the large-scale circulation, *Monthly Weather Review*, *127*(3), 409-431.

Lenters, J. D., M. T. Coe, and J. A. Foley (2000), Surface water balance of the continental United States, 1963-1995: Regional evaluation of a terrestrial biosphere model and the NCEP/NCAR reanalysis, *Journal of Geophysical Research-Atmospheres*, *105*(D17), 22393-22425.

Li, W. H., and R. Fu (2004), Transition of the large-scale atmospheric and land surface conditions from the dry to the wet season over Amazonia as diagnosed by the ECMWF re-analysis, *Journal of Climate*, *17*(13), 2637-2651.

Li, W. H., and R. Fu (2006), Influence of cold air intrusions on the wet season onset over Amazonia, *Journal of Climate*, *19*(2), 257-275.

Li, W. H., R. Fu, and R. E. Dickinson (2006), Rainfall and its seasonality over the Amazon in the 21st century as assessed by the coupled models for the IPCC AR4, *Journal of Geophysical Research-Atmospheres*, *111*(D2).

Li, W. H., R. Fu, R. I. N. Juarez, and K. Fernandes (2008), Observed change of the standardized precipitation index, its potential cause and implications to future climate change in the Amazon region, *Philosophical Transactions of the Royal Society B-Biological Sciences*, *363*(1498), 1767-1772.

Liebmann, B., and J. A. Marengo (2001), Interannual variability of the rainy season and rainfall in the Brazilian Amazon basin, *Journal of Climate*, *14*(22), 4308-4318.

Liebmann, B., S. J. Camargo, A. Seth, J. A. Marengo, L. M. V. Carvalho, D. Allured, R. Fu, and C. S. Vera (2007), Onset and end of the rainy season in South America in observations and the ECHAM 4.5 atmospheric general circulation model, *Journal of Climate*, *20*(10), 2037-2050.

Liu, N., H. X. Chen, and L. G. Lu (2007), Teleconnection of IOD signal in the upper troposphere over southern high latitudes, *Journal of Oceanography*, *63*(1), 155-157.

Malhi, Y., E. Pegoraro, A. D. Nobre, M. G. P. Pereira, J. Grace, A. D. Culf, and R. Clement (2002), Energy and water dynamics of a central Amazonian rain forest, *Journal of Geophysical Research-Atmospheres, 107*(D20), DOI: 10.1029/2001JD000623.

Malhi, Y., and J. Wright (2004), Spatial patterns and recent trends in the climate of tropical rainforest regions, *Philosophical Transactions of the Royal Society of London Series B-Biological Sciences*, *359*(1443), 311-329.

Mann, H. B. (1945), Nonparametric tests against trend, *Econometrica*, *13*(3), 245-259.

Mantua, N. J., S. R. Hare, Y. Zhang, J. M. Wallace, and R. C. Francis (1997), A Pacific interdecadal climate oscillation with impacts on salmon production, *Bulletin of the American Meteorological Society*, *78*(6), 1069-1079.

Marengo, J. A., B. Liebmann, V. E. Kousky, N. P. Filizola, and I. C. Wainer (2001), Onset and end of the rainy season in the Brazilian Amazon Basin, *Journal of Climate*, *14*(5), 833-852.

Marengo, J. A. (2004), Interdecadal variability and trends of rainfall across the Amazon basin, *Theoretical and Applied Climatology*, *78*(1-3), 79-96.

Marengo, J. A. (2005), Characteristics and spatio-temporal variability of the Amazon River Basin Water Budget, *Climate Dynamics*, *24*(1), 11-22.

Matsuyama, H. (1992), The water budget in the Amazon River basin during the FGGE period, *Journal of the Meteorological Society of Japan*, *70*(6), 1071-1084.

Mestas-Nunez, A. M., and A. J. Miller (2006), Interdecadal variability and climate change in the eastern tropical Pacific: A review, *Progress in Oceanography*, *69*(2-4), 267-284.

Mo, K. C. (2000), Relationships between low-frequency variability in the Southern Hemisphere and sea surface temperature anomalies, *Journal of Climate*, *13*(20), 3599-3610.

Mo, K. C., and J. N. Paegle (2001), The Pacific-South American modes and their downstream effects, *International Journal of Climatology*, *21*(10), 1211-1229.

Muller, G. V., T. Ambrizzi, and M. N. Nunez (2005), Mean atmospheric circulation leading to generalized frosts in central southern South America, *Theoretical and Applied Climatology*, *82*(1-2), 95-112.

Muller, G. V., and T. Ambrizzi (2007), Teleconnection patterns and Rossby wave propagation associated to generalized frosts over southern South America, *Climate Dynamics*, *29*(6), 633-645.

Neelin, J. D., D. S. Battisti, A. C. Hirst, F. F. Jin, Y. Wakata, T. Yamagata, and S. E. Zebiak (1998), ENSO theory, *Journal of Geophysical Research-Oceans*, *103*(C7), 14261-14290.

NoguesPaegle, J., and K. C. Mo (1997), Alternating wet and dry conditions over South America during summer, *Monthly Weather Review*, *125*(2), 279-291.

Oliveira, A. S. (1986), Interactions between South American frontal systems and convection in the Amazon, Master's thesis, 115 pp, Instituto Nacional de Pesquisas Epaciais, São José dos Campos.

Ometto, J., A. D. Nobre, H. R. Rocha, P. Artaxo, and L. A. Martinelli (2005), Amazonia and the modern carbon cycle: lessons learned, *Oecologia*, *143*(4), 483-500.

Paegle, J. N., and K. C. Mo (2002), Linkages between summer rainfall variability over south America and sea surface temperature anomalies, *Journal of Climate*, *15*(12), 1389-1407.

Pezza, A. B., and T. Ambrizzi (2005), Dynamical conditions and synoptic tracks associated with different types of cold surge over tropical South America, *International Journal of Climatology*, *25*(2), 215-241.

Pezza, A. B., I. Simmonds, and J. A. Renwick (2007), Southern Hemisphere cyclones and anticyclones: Recent trends and links with decadal variability in the Pacific Ocean, *International Journal of Climatology*, *27*(11), 1403-1419.

Raia, A., and I. F. D. Cavalcanti (2008), The Life Cycle of the South American Monsoon System, *Journal of Climate*, *21*(23), 6227-6246.

Rao, V. B., I. F. A. Cavalcanti, and K. Hada (1996), Annual variation of rainfall over Brazil and water vapor characteristics over South America, *Journal of Geophysical Research-Atmospheres*, *101*(D21), 26539-26551.

Rayner, N. A., P. Brohan, D. E. Parker, C. K. Folland, J. J. Kennedy, M. Vanicek, T. J. Ansell, and S. F. B. Tett (2006), Improved analyses of changes and uncertainties in sea surface temperature measured in situ sice the mid-nineteenth century: The HadSST2 dataset, *Journal of Climate*, *19*(3), 446-469.

Renwick, J. A., and M. J. Revell (1999), Blocking over the South Pacific and Rossby wave propagation, *Monthly Weather Review*, *127*(10), 2233-2247.

Roads, J., and A. Betts (2000), NCEP-NCAR and ECMWF reanalysis surface water and energy budgets for the Mississippi River basin, *Journal of Hydrometeorology*, *1*(1), 88-94.

Ropelewski, C. F., and M. S. Halpert (1987), Global and Regional Scale Precipitation Patterns Associated with the El-Niño Southern Oscillation, *Monthly Weather Review*, *115*(8), 1606-1626.

Rutter, A. J., A. J. Morton, and P. C. Robins (1975), Predictive model of rainfall interception forests.2. Generalization of model and comparison with observations in some coniferous and hardwood stands, *Journal of Applied Ecology*, *12*(1), 367-380.

Saji, N. H., B. N. Goswami, P. N. Vinayachandran, and T. Yamagata (1999), A dipole mode in the tropical Indian Ocean, *Nature*, *401*(6751), 360-363.

Saji, N. H., and T. Yamagata (2003), Possible impacts of Indian Ocean Dipole mode events on global climate, *Climate Research*, *25*(2), 151-169.

Saji, N. H., T. Ambrizzi, and S. E. T. Ferraz (2005), Indian Ocean Dipole mode events and austral surface air temperature anomalies, *Dynamics of Atmospheres and Oceans*, *39*(1-2), 87-101.

Sen, P. K. (1968), Estimates of regression coefficient based on Kendalls tau, *Journal of the American Statistical Association*, *63*(324), 1379-&.

Seneviratne, S. I., P. Viterbo, D. Luthi, and C. Schar (2004), Inferring changes in terrestrial water storage using ERA-40 reanalysis data: The Mississippi River basin, *Journal of Climate*, *17*(11), 2039-2057.

Silva, V. B. S., V. E. Kousky, W. Shi, and R. W. Higgins (2007), An improved gridded historical daily precipitation analysis for Brazil, *Journal of Hydrometeorology*, *8*(4), 847-861.

Sombroek, W. (2001), Spatial and temporal patterns of Amazon rainfall - Consequences for the planning of agricultural occupation and the protection of primary forests, *Ambio*, *30*(7), 388-396.

Tian, H. Q., J. M. Melillo, D. W. Kicklighter, A. D. McGuire, J. V. K. Helfrich, B. Moore, and C. J. Vorosmarty (1998), Effect of interannual climate variability on carbon storage in Amazonian ecosystems, *Nature*, *396*(6712), 664-667.

Vera, C., G. Silvestri, V. Barros, and A. Carril (2004), Differences in El Nino response over the Southern Hemisphere, *Journal of Climate*, *17*(9), 1741-1753.

Vera, C. S., and P. K. Vigliarolo (2000), A diagnostic study of cold-air outbreaks over South America, *Monthly Weather Review*, *128*(1), 3-24.

von Randow, C., A. O. Manzi, B. Kruijt, P. J. de Oliveira, F. B. Zanchi, R. L. Silva, M. G. Hodnett, J. H. C. Gash, J. A. Elbers, M. J. Waterloo, F. L. Cardoso, and P. Kabat (2004), Comparative measurements and seasonal variations in energy and carbon exchange over forest and pasture in South West Amazonia, *Theoretical and Applied Climatology*, *78*(1-3), 5-26.

Vorosmarty, C. J., C. J. Willmott, B. J. Choudhury, A. L. Schloss, T. K. Stearns, S. M. Robeson, and T. J. Dorman (1996), Analyzing the discharge regime of a large tropical river through remote sensing, ground-based climatic data, and modeling, *Water Resources Research*, *32*(10), 3137-3150.

Wallace, J. M., G. H. Lim, and M. L. Blackmon (1988), Relationship between cyclone tracks, anticyclone tracks and baroclinic wave-guides, *Journal of the Atmospheric Sciences*, *45*(3), 439-462.

Wang, B., and Q. H. Ding (2006), Changes in global monsoon precipitation over the past 56 years, *Geophysical Research Letters*, *33*(6).

Wang, H., and R. Fu (2002), Cross-equatorial flow and seasonal cycle of precipitation over South America, *Journal of Climate*, *15*(13), 1591-1608.

Webster, P. J., A. M. Moore, J. P. Loschnigg, and R. R. Leben (1999), Coupled ocean-atmosphere dynamics in the Indian Ocean during 1997-98, *Nature*, *401*(6751), 356-360.

Wilks, D. S. (2006), *Statistical Methods in the Attmospheric Sciences*, Second ed., 630 pp., Elsevier.

Yu, H., R. Fu, R. E. Dickinson, Y. Zhang, M. Chen, and H. Wang (2007), Interannual variability of smoke and warm cloud relationships in the Amazon as inferred from MODIS retrievals, *Remote Sensing of Environment*, *111*(4), 435-449.

Zeng, N. (1999), Seasonal cycle and interannual variability in the Amazon hydrologic cycle, *Journal of Geophysical Research-Atmospheres, 104*(D8), 9097-9106, DOI: 10.1029/1998JD200088.

Zhang, Y., R. Fu, H. B. Yu, R. E. Dickinson, R. N. Juarez, M. A. Chin, and H. Wang (2008), A regional climate model study of how biomass burning aerosol impacts land-atmosphere interactions over the Amazon, *Journal of Geophysical Research-Atmospheres*, *113*(D14).

Zhang, Y., R. Fu, H. Yu, H. Qian, R. E. Dickinson, M. A. F. Silva Dias, P. L. D. Silva Dias, and K. Fernandes (2009), Impact of biomass burning aerosol on the monsoon circulation transition over Amazonia, *Geophysical Research Letters*, *36*